AFRL-SR-BL-TR-98-

0264

REPORT DOCUMENTATION PAGE

1. AGENCY USE ONLY (Leave blank)	2. REPORT DATE	3. REPORT TYPE AND DATES COVERED
	January 1998	Final Technical Report 7-1-94/6-30-97

4. TITLE AND SUBTITLE
"The Mechanical Response of Cross-Ply and Angle-Ply Ceramic Composite Laminates"

5. FUNDING NUMBERS
AF F49620-94-1-0344

6. AUTHOR(S)
Alex S. Selvarathinam and Y. Jack Weitsman

7. PERFORMING ORGANIZATION NAME(S) AND ADDRESS(ES)
Department of Mechanical and Aerospace Engineering
and Engineering Science
The University of Tennessee
Knoxville, TN 37996-2030

8. PERFORMING ORGANIZATION REPORT NUMBER
MAES98-1.0-CM

9. SPONSORING/MONITORING AGENCY NAME(S) AND ADDRESS(ES)
Air Force Office of Scientific Research
Directorate of Aerospace and Materials Sciences
AFOSR/NA
110 Duncan Ave., Suite B-115
Bolling AFB, DC 20332-8080

10. SPONSORING/MONITORING AGENCY REPORT NUMBER
94-1-0344

11. SUPPLEMENTARY NOTES

12a. DISTRIBUTION/AVAILABILITY STATEMENT
Unlimited

12b. DISTRIBUTION CODE

13. ABSTRACT (Maximum 200 words)

This report summarizes the investigations performed under Contract AF F49620-94-1-0344, titled, "The Mechanical Response of Cross-Ply and Angle-Ply Ceramic Composite Laminates".

The study of deformation and fracture in cross-ply $[0_m^\circ/90_n^\circ]_s$ fiber-reinforced ceramic laminates consisted of two parts. The first study aimed at predicting the macro-level stress-strain response and included experimental and analytical components. The second study focused on detailed failure mechanisms, striving to determine analytically the advent of failure in the 90° plies and its progression into the 0° layers. Both foregoing investigations employed fracture energy considerations to determine failure.

The study of failure in off-axis and angle-ply laminates utilized detailed fracture mechanics analyses to compute both singular and far-field stresses associated with cracks impinging on inclined bi-material interfaces. The results provided a rational explanation for observed response.

14. SUBJECT TERMS	15. NUMBER OF PAGES
Ceramic Composites, Multi-dimensional Reinforcement, Failure Mechanisms.	36
	16. PRICE CODE

17. SECURITY CLASSIFICATION OF REPORT	18. SECURITY CLASSIFICATION OF THIS PAGE	19. SECURITY CLASSIFICATION OF ABSTRACT	20. LIMITATION OF ABSTRACT
Unclassified	Unclassified	Unclassified	Unlimited

FINAL TECHNICAL REPORT

"THE MECHANICAL RESPONSE OF CROSS-PLY AND ANGLE-PLY CERAMIC COMPOSITE LAMINATES"

By

Alex S. Selvarathinam and Y. Jack Weitsman

Prepared for: **Air Force Office of Scientific Research**
Bolling AFB, DC

AFOSR/NA
Aerospace and Materials Sciences Directorate
Contract AF F49620-94-1-0344

Report MAES98-1.0-CM
January 1998

Mechanical and Aerospace Engineering
and Engineering Science
THE UNIVERSITY OF TENNESSEE
Knoxville, TN 37996-2030

ABSTRACT

This report summarizes the investigations performed under Contract AF F49620-94-1-0344, titled, "The Mechanical Response of Cross-Ply and Angle-Ply Ceramic Composite Laminates".

The study of deformation and fracture in cross-ply $[0^{\circ}_{m}/90^{\circ}_{n}]_{s}$ fiber-reinforced ceramic laminates consisted of two parts. The first study aimed at predicting the macro-level stress-strain response and included experimental and analytical components. The second study focused on detailed failure mechanisms, striving to determine analytically the advent of failure in the 90° plies and its progression into the 0° layers. Both foregoing investigations employed fracture energy considerations to determine failure.

The study of failure in off-axis and angle-ply laminates utilized detailed fracture mechanics analyses to compute both singular and far-field stresses associated with cracks impinging on inclined bi-material interfaces. The results provided a rational explanation for observed response.

1. Introduction

Ceramic materials exhibit superior capability to withstand high temperatures but their performance is inhibited by excessive brittleness. This brittleness can be ameliorated by reinforcement with relatively ductile ceramic fibers, resulting in about a six-fold increase in failure strains.

However, since the above improvement in ductility occurs only in the fiber-direction, multi-directional reinforcement is required to enhance the performance of ceramics for realistic technical applications.

Such enhancement was noted in several experimental investigations regarding the stress-strain response of cross-ply and angle-ply ceramic laminates [1], [2], as shown in Figs. 1-3, with separate observations of detailed failure mechanisms sketched in Figs. 4 and 5. However, comprehensive rational analyses seem to be lacking at the present time. Several attempts to model the behavior of cross-ply ceramic laminates [4], [5] incorporated ad-hoc assumptions that are extraneous to the analytical formulations, and no analysis is available to explain the observed behaviors of off-axis and angle-ply laminates.

2. Cross-Ply Laminates

2.1 Stress-Strain Response, Data and Model

2.1.1 Experimental

The experiments involved the testing of two SiC/CAS cross-ply laminates, a $[0_2^\circ/90_2^\circ]_s$ lay-up that was utilized for characterization and model construction, and a $[0_2^\circ/90_4^\circ]_s$ lay-up that was tested for model verification. Recordings of stress-strain response under the application of a constant strain-rate was accompanied by in-situ observations of micro-cracks in both the 0° and 90° ply groups, employing a closed circuit microscope system with a 750X magnification, as sketched in Fig. 6. Typical microscopic observations are shown in Fig. 7, while stress-strain curves with counts of crack densities correlated to strain levels, as shown in Figs. 8 and 9.

In view of the well known presence of interfacial slippage between fibers and matrix in unidirectionally reinforced ceramics, a special, custom made device was constructed to evaluate slippage between the 0° and 90° ply groups. A sketch of this "mini-shear" fixture is given in Fig. 10. In this manner it was possible to observe damage progression at the 0°/90° interface, as exhibited in Fig. 11 and record load-displacement data as shown in Fig. 12. These data enable the incorporation of inter-ply slip within the analytical formulation.

2.1.2 Analytical

The analysis employed an extended shear-lag formulation to model the response of cross-ply laminates through the correlation of stress-strain response with the increase in damage.

For this purpose, the stress-strain behavior of the 0° plies was expressed in bi-linear form as shown in Fig. 13. This representation, which accounted for the growing damage within the 0° plies, necessitated the establishment of a non-linear shear lag model. Note that the foregoing damage in the 0° plies, in the form of fiber-bridged matrix cracks, interfacial fiber/matrix slippage and fiber breakage, received ample attention in published literature (see e.g. [6], [7] and references listed there in).

In addition, the non-linear shear-lag model also accounted for inter-laminar slip, by delimiting interlaminar shear stresses to within the range $\tau_s<\tau_s^*$. The value of τ_s^* was computed from the mini shear fixture data shown in Fig. 12.

The above considerations resulted in a shear-lag model with geometry and "characteristic cell" shown in Fig. 14, where the 0°/90° interface divides into the three sub-regions shown in Fig. 15. In that figure the transverse crack in the 90° ply-group is located at $x = L$, slippage occurs over $L - l_s \le x \le L$ and non-linear stress response in the 0° plies occurs within $x^* < x < L$ (or

$x^{*1} < x < L$ for a relatively shorter slip region). It follows that the formulation contains two additional unknowns, l_s and x^* (or x^{*1}), that are not present in established shear-lag formulations [8], [9]. These unknowns are associated with two conditions, namely $\tau_s(L - l_s) = \tau_s^*$ and $\sigma_x^{(o)}(x^*) = \sigma_o$, (or $\sigma_x^{(o)}(x^{*1}) = \sigma_o$) where τ_s^* is the aforementioned limiting value of the interfacial shear stress and σ_o is the "yield stress" shown in Fig. 13. Consequently, the shear-lag formulation results in a set of simultaneous, non-linear algebraic equations that involve l_s and x^* (or l_s and x^{*1}) whose solution provides the average normal stresses $\sigma_x^{(o)}$ and σ_x^{90} in the 0° and 90° ply groups, as well as for the interfacial shear stress τ between the above plies. These equations must be solved iteratively.

The advent of new transverse cracks within the inner, 90° ply group is determined by means of a "global" fracture energy criterion. Accordingly, the complementary strain-energy U^* is evaluated for two configurations, as shown in Fig. 16, leading to an available fracture energy expressed by

$$J_a = \frac{2U^*(L) - U^*(2L)}{2h_1} \qquad (1)$$

New transverse cracks are assumed to "pop in" when $J_a = J_c$, with J_c denoting the critical value. Values for J_c are listed in the literature to within experimental scatter.

2.1.3 Results

The predictive capability of the enhanced shear-lag model was examined at first through comparisons with the response of the $[0_2^\circ/90_2^\circ]_s$ lay-up. Several parametric values of J_c and τ_s^*, all within the range of data scatter ($12\ J/m^2 \le J_c \le 30\ J/m^2$, $35\ MPa < \tau_s < 55\ MPa$), were employed to compare predicted and recorded stress-strain curves as well as densities of transverse cracks in the 90° ply group. Twelve such case studies were investigated, involving several replicate specimens. Typical results and comparisons are shown in Figs. 17-19.

Similar results including twelve additional case studies, were evaluated for $[0_2^\circ/90_4^\circ]_s$ lay-ups, with typical comparisons exhibited in Figs. 20-22.

Inspection of the above figures indicates that $\tau_s \sim 55MPa$ and $J_c \sim 12J/m^2$ yield the best agreement between model and experiment. The above values fall well within the acceptable range of experimental measurements.

It should be noted that in order to achieve reasonable agreement between model and data it was essential to incorporate both interlaminar slip and non-linearity of the 0° ply group behavior into the model. Although not shown here, the omission of even one of the above phenomena resulted in wide departures from data and observations.

2.2 Failure Mechanisms in Cross-Ply Laminates

The objective of this analytical work was to account for individual failure mechanisms in both 0° and 90° ply groups and evaluate the evolution of various failure scenarios. These scenarios included the introduction of additional cracks with the 90° ply group and the propagation of the above cracks into the outer 0° plies. Comparative levels of available and required fracture energies were evaluated for distinct circumstances to serve as indicators for the preferred scenario. All comparisons were performed for representative volume elements and utilized approximate solutions that employ "enhances" shear-lag models. These models incorporate slips and interlaminar shear at the 0°/90° interfaces, as well as slip and interfacial shears at the fiber/matrix interfaces within the 0° plies.

The first comparison was evaluated for the scenarios shown in Fig. 23, where the transition from state A to state B was compared with the transition from state A to state C.

The transition A→B involves softening of the 90° plies by the insertion therein of additional transverse cracks as well as by generating additional slip regions emanating from the tips of those newly created transverse cracks. On the other hand, the transition A→C generates additional slips at the fiber/matrix interfaces within the 0° plies. Note that in the transition A→C, the fully developed transverse cracks remain bridged by intact fibers in the 0° plies.

The second comparison is provided for the transition from state C (shown in Fig. 23) to states D and E shown in Fig. 24.

The transition C→D is akin to the transition A→B except that it occurs on the background of transverse cracks that span the entire 0°/90° laminate. On the other hand, the transition C→E involves the insertion of additional fiber-bridged matrix cracks in the 0° plies.

The required levels of fracture energy are taken to be $G_c^{(90)}$ and G_c^m, where $G_c^{(90)}$ is the critical level for transverse fracture and G_c^m is the critical fracture energy of the ceramic matrix.

The computations were based upon the following data for SiC/CAS composites:
$h^{(90)} = h^{(0)} = 0.413 \times 10^{-3}$m, $E^{(90)} = 117$ GPa, $E^{(0)} = 124$ GPa, $G_{yz} = 55$ GPa, $G_{xz} = 37$ GPa, $\tau_s = 45$ MPa, $\tau_s^* = 15$ MPa, $G_c^{90} = 20$ N/m, $G_c^m = 40$ N/m, $a = 7.5$ μm, $E_f = 165$ GPa, $E_m = 97$ GPa, and $V_f = 0.4$. In the above τ_s refers to interlaminar shear strength and τ_s^* to the interfacial fiber/matrix shear strength. The initial transverse crack spacing was chosen to be L = 64h. It turned out that for the specific lay-up considered herein either of the transitions A→B or A→Cwas possible for $\sigma = 60$ MPa but the transitions C→E was clearly preferable at $\sigma = 100$ MPa. Thus, the experimental observation, noted in Fig. 9, that the density of transverse cracks in the 90° -plies is quickly overtaken by fiber-bridged matrix cracks in the 0° -plies might be explained from an energy point of view as suggested by the analysis performed herein.

3. Off-Axis and Angle-Ply Laminates

The meager amount of stress-strain data for angle-ply and off-axis fiber-reinforced ceramic composites, as shown in Figs. 2 and 3, demonstrate that angle-ply laminates possess markedly higher comparative levels of both failure strains and failure stresses.

Observations of failure progression, shown schematically in Figs. 25 and 26, indicate that failure in both above lay-ups consists of matrix cracks oriented perpendicularly to the load direction, which are bridged by oblique fibers. However, the foregoing cracks proceed to branch out along the fiber/matrix interfaces into shaped formations only for off-axis reinforcement, while such branchings seem to be arrested in angle-ply lay-ups.

3.1 Off-Axis Laminates

An explanation for the above mentioned crack branchings in the off-axis circumstance was provided by means of a finite element analysis of the nine-crack geometry shown in Fig. 27. Preliminary studies had shown that the response of the central crack "C" is not affected by interactions with additional cracks.

Computations were performed for equal fiber and matrix volume fractions $V_f = V_m = 0.5$, with a moduli ratio $E_f/E_m = 1.78$ and Poisson's ratios $\nu_m = 0.35$ and $\nu_f = 0.2$. The main purpose of FEM analysis was to evaluate the tractions along the obliquely oriented fiber/matrix interfaces near and away from the tips of the horizontal matrix cracks.

The computations of the above interfacial tractions encountered some unexpected difficulty upon approaching the crack tip. While no oscillatory singularity was expected to occur for the foregoing material properties and an oblique angle $\psi = 30°$, finite element computations had nevertheless contained a sign reversal with diminishing element size.

A resolution of the apparent contradiction between finite element computational results and singularity considerations was achieved by conducting a detailed investigation of the singular field near the tip of a crack impinging on a bi-linear interface, with regions i = 1,2,3 as shown in Fig. 28.

Employment of the eigen-function analysis, as formulated by Fenner, yielded the following expressions for the stresses and displacements near the tip of the crack shown in Fig. 28:

$$\sigma_{irr} = \frac{Q_1}{r^{1-\lambda_1}} f_{1rr}(\lambda_1,\theta) + \frac{Q_2}{r^{1-\lambda_2}} f_{2rr}(\lambda_2,\theta) + Q_3 f_{3rr}(1,\theta)$$

$$\sigma_{i\theta\theta} = \frac{Q_1}{r^{1-\lambda_1}} f_{1\theta\theta}(\lambda_1,\theta) + \frac{Q_2}{r^{1-\lambda_2}} f_{2\theta\theta}(\lambda_2,\theta) + Q_3 f_{3\theta\theta}(1,\theta)$$

$$\sigma_{ir\theta} = \frac{Q_1}{r^{1-\lambda_1}} f_{1r\theta}(\lambda_1,\theta) + \frac{Q_2}{r^{1-\lambda_2}} f_{2r\theta}(\lambda_2,\theta) + Q_3 f_{3r\theta}(1,\theta) \qquad (2)$$

$$u_{ir} = \frac{Q_1 r^{\lambda_1}}{2G_i} g_{1r}(\lambda_1,\theta) + \frac{Q_2 r^{\lambda_2}}{2G_i} g_{2r}(\lambda_2,\theta)$$

$$u_{i\theta} = \frac{Q_1 r^{\lambda_1}}{2G_i} g_{1\theta}(\lambda_1,\theta) + \frac{Q_2 r^{\lambda_2}}{2G_i} g_{2\theta}(\lambda_2,\theta)$$

where r and θ are polar coordinates λ_1 and λ_2 are the powers of the singularity with Q_1 and Q_2 the corresponding "amplification factors" (akin to stress intensity factors). Q_3 is the factor associated with the leading non-singular term.

The foregoing material properties yielded $\lambda_1 = 0.509$ and $\lambda_2 = 0.569$. Subsequently, was possible to determine Q_1, Q_2 and Q_3 by matching the far field solution, obtained through FEM analysis, with near field values, along contours surrounding the crack tip.

It turned out that the aforementioned sign reversal in the interfacial tractions is consistent with the near field formulation listed in eqns. (2). However, this sign reversal was due to the fact that the factors Q_1 and Q_2 are of opposing signs ($Q_1 > o$ while $Q_2 < o$), and no further oscillation occurred upon approaching the crack tip.

The above clarification allows for the generation of the entire solution for the interfacial tractions along the fiber/matrix boundaries, along the rays at $\phi = -\psi = 30°$ that originate at the crack ties . The results are plotted in Figs. 29 and 30, indicating tensile tractions along the portions L1 and R2 with

compression along the portions L2 and R1 of the aforementioned boundaries. The foregoing sign change occurs along R1 (and L2) upon approaching the crack tips, as shown in detail in Fig. 31.

The presence of tensile tractions that are predicted to occur adjacently to the crack tips along the interfaces L1 and R2 explain the debondings that are observed in such locations, thereby the " " shaped cracks sketched in Fig. 25b.

3.2 Angle-Ply Laminates

Angle-ply lamination, i.e. a $[\pm\psi]_s$ lay-up, constrains the deformation of the individual off-axis plies, oriented in the $+\psi$ and $-\psi$ directions, to exclude shear-strains. This exclusion is accompanied by ply-level shear stresses that are absent in the off-axis laminates discussed in sub-section 3.1

An accounting for the above mentioned mutual constraint in the $[\pm 30^\circ]_s$ laminate was achieved by letting the remote horizontal displacement along the boundaries $x = \pm W = \pm 32a$ be $U = -0.252V$, as shown in Fig. 32. Those boundary conditions, which stem from elementary considerations of laminated plate analysis, replaced the traction free boundary, conditions employed in sub-section 3.1.

As may have been expected, the characteristics of the singular solution near the tips of the central crack "C" remain unaffected by the above change in remote boundary conditions. Thus, while the amplitudes Q_1, Q_2 and Q_3 differed, the eigen values λ_1 and λ_2 remained unchanged and the complete solution for the , say, $\psi = -30^\circ$ plies bore a strong resemblance to the results shown in Figs. 29-31. The results for the angle-ply lay-up are exhibited in Figs. 33-35, with comparative plots for the off-axis case marked by the letter "O" in Fig. 35.

Accordingly, tensile and compressive interfacial tractions continue to prevail along portions of the boundaries $L1^-$ and $R2^-$, $L2^-$ and $R1^-$, respectively of the plies oriented at $\psi = -30^\circ$ as before. By symmetry, the same tensile and compressive tractions occur along the boundaries $(R1^+, L2^+)$ and $(R2^+, L1^+)$, respectively, of the plies oriented at $\psi = +30^\circ$ as before.

Upon viewing the combined $[\pm 30^\circ]_s$ lay-up shown in Fig. 36 it becomes evident that individual delamination along the boundaries $L1^-$,$R2^-$ and $L2^+$, $R1^+$ are inhibited by the presence of adjacent plies at opposite fiber orientations. This limitation is due to the fact that any such delamination cannot proceed freely without cutting into the fibers in the adjacent layers. Consequently, angle ply lamination inhibits damage and increases the load carrying capacity of the composite.

4. Concluding Remarks

The research reported herein provided several rational explanations, based upon mechanics analyses, for observed responses of multi-directionally fiber reinforced ceramic composites. Considerations were restricted to reinforcement by straight and continuous fibers. Interlaminar slip between distinctly oriented plies was noted to play a significant role in the overall response of ceramic composite laminates.

Further experimental data, including observations of damage evolution, are necessary to construct a predictive model for the stress-strain response of angle-ply laminates. Such data are not available at the present time.

It is deemed that the response of woven fabric reinforced ceramic composites is much too complex to be modeled through concepts of fracture mechanics, as reported herein, and that an approach based upon continuum damage mechanics may be more appropriate.

References

[1] Kim, R. Y., "Experimental Observation of Progressive Damage in SiC/Glass-Ceramic Composites", ACSS Proceedings of the 16th Annual Conference on Composites and Advanced Ceramics Material, Vol. 13, #7-8 (1992), pp. 281-300.

[2] Nardone, V. C. and Prewo, K. M., "Tensile Performance of Carbon-Fibre-Reinforced Glass", *Journal of Materials Science*, 23 (1988), pp. 168-180.

[3] Cady, C., Heredia, F. E., and Evans, A. G., "In-Plane Mechanical Properties of Several Ceramic Matrix Composites", *Journal of American Ceramic Society*, Vol. 78, 1995, pp. 2065-2078.

[4] Bhatt, R. T. and Phillips, R. E., "Laminate Behavior for SiC Fiber-Reinforced Reaction-Bonded Silicon Nitride Matrix Composites", NASA Technical Memorandum 101250.

[5] Kuo, W. -S and Chou, T. -W., "Modeling of Damage in Ceramic-Matrix Cross-Ply Composites", AMD-Vol. 142/MD-Vol. 34, Damage Mechanics and Localization (1992), (Ju, J. W., Editor) ASME, New York, pp. 97-107.

[6] Weitsman, Y. J. and Zhu, H. "Multi-Fracture of Ceramic Composites", *J. Mech. Phys. Solids* Vol. 41, No. 2, (1993), pp. 351-388.

[7] Zhu, H. and Weitsman, Y. J. , "The progression of Failure Mechanisms in Unidirectionally Reinforced Ceramic Composites", *J. Mech. Phys. Solids* Vol. 42, No. 10, (1994), pp. 1601-1632.

[8] Nuismer, R. J. and Tan, S. C., "Constitutive Relations of a Cracked Composite Lamina", *Journal of Composite Materials*, Vol. 22 - April (1988), pp. 306-321.

[9] Tan, S. C. and Nuismer, R. J., "A Theory for Progressive Matrix Cracking in Composite Laminates", *Journal of Composite Materials*, Vol. 23 - October (1989), pp. 1029-1047.

[10] Bhatt, R. T. and Phillip, R. E.: Laminate Behavior for SiC Fiber-Reinforced Reaction-Bonded Silicon Nitride Matrix Composites, NASA Technical Memorandum 101350, 1988.

Appendix: Articles Completed Under Contract AF F49620-94-1-0344

1. D. Erdman: "The Mechanical Response of Cross-Ply Ceramic Composites", Ph.D. Thesis, The University of Tennessee, December 1995.

2. Yu, N. Zhu, H. and Weitsman, Y., (1995). "On Damage Evolution of Cross-Ply Ceramic Composites," in *Ceramic Engineering & Science Proceedings*, 16, 4, G. N. Pfendt (ed.), The American Ceramic Society, pp. 361-368.

3. Weitsman, Y., (1995). "Multi-fracture Processes in Ceramic Composites", Proceedings of the IUTAM-ISIMM Symposium, Nottingham, U.K., Aug. 30-Sept. 3, 1994, Vol. 39, pp. 293-298.

4. Selvarathinam, A. S., (1996). "Fracture in Unidirectional Off-Axis Ceramic Matrix Composite", Contract Technical Report No. MAES96-4.0-CM, Department of Mechanical and Aerospace Engineering and Engineering Science, The University of Tennessee, Knoxville 37996-2030.

5. Selvarathinam, A. S., Weitsman, Y. J. (1997). "Fracture in Angle-Ply Ceramic Matrix Composites", Contract Technical Report No. MAES97-2.0-CM, Department of Mechanical and Aerospace Engineering and Engineering Science, The University of Tennessee, Knoxville 37996-2030.

6. Selvarathinam, A. S., Weitsman, Y. J. (1997). "Fracture in Off-Axis and Angle-Ply Fiber Reinforced Ceramics", Eleventh International Confrence on Composite Materials (ICCM-11), Gold Coast, Australia, July 14-18, 1997, Vol. II, pp. 694-702.

7. Erdman, D. and Weitsman, Y. (1998). "The Multi-Fracture Response of Cross-Ply Ceramic Composites," scheduled to appear in the September 1998 issure of the *International Journal of Solids & Structure.*

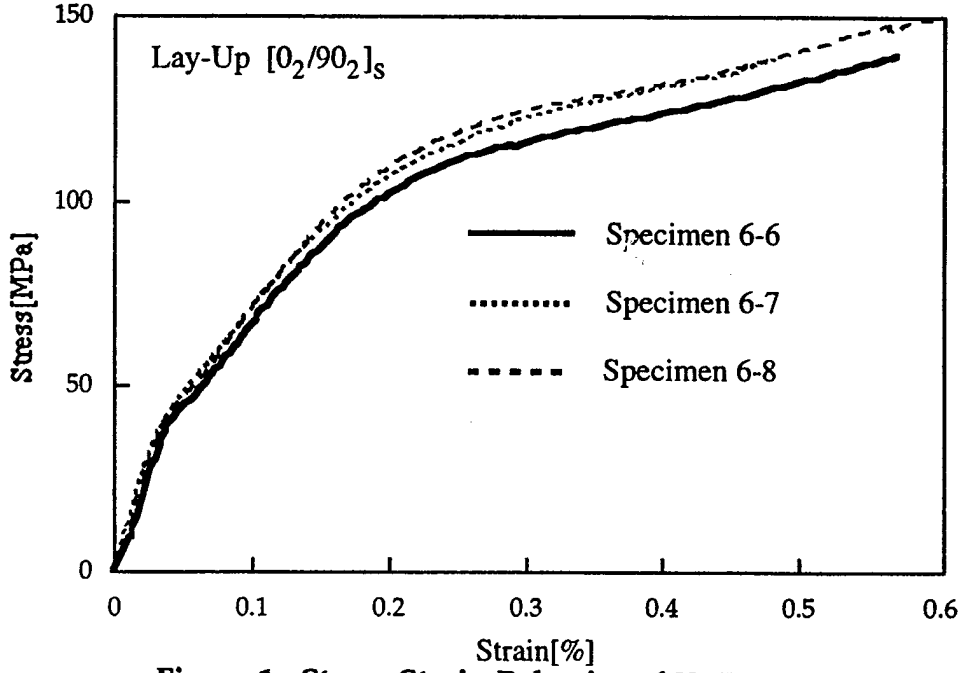

Figure 1. Stress-Strain Behavior of $[0_2/90_2]_s$ Laminate

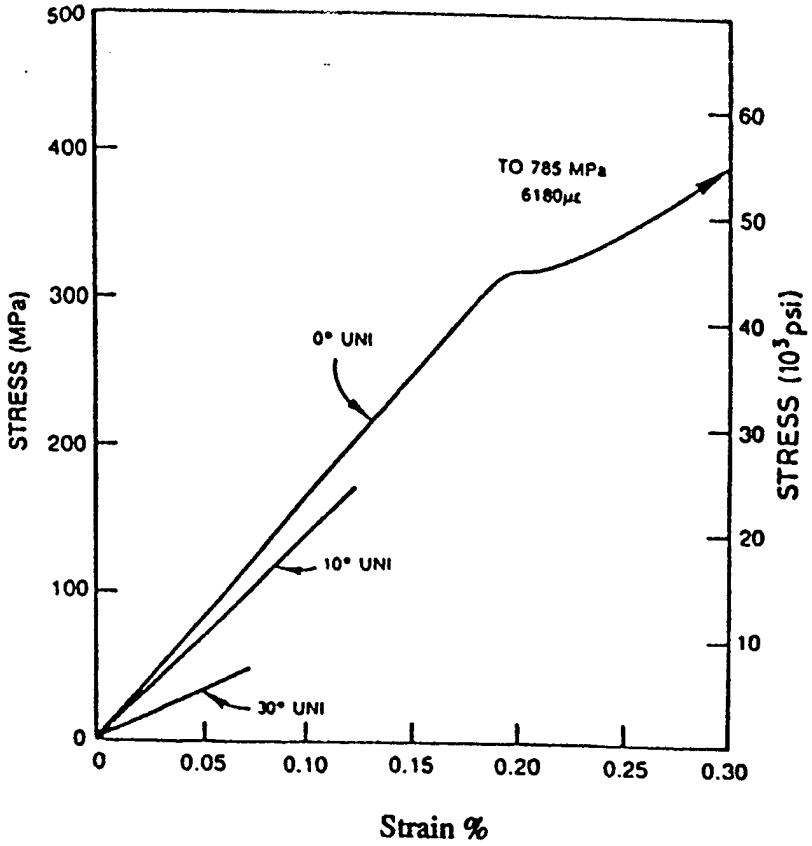

Figure 2. The Stress-Strain Response of Unidirectionally Reinforced, Off-Axis, HMU 7740 Composite (After Ref. [2]). Note the Brittle-Like Behavior, when Compared with Figure 3.

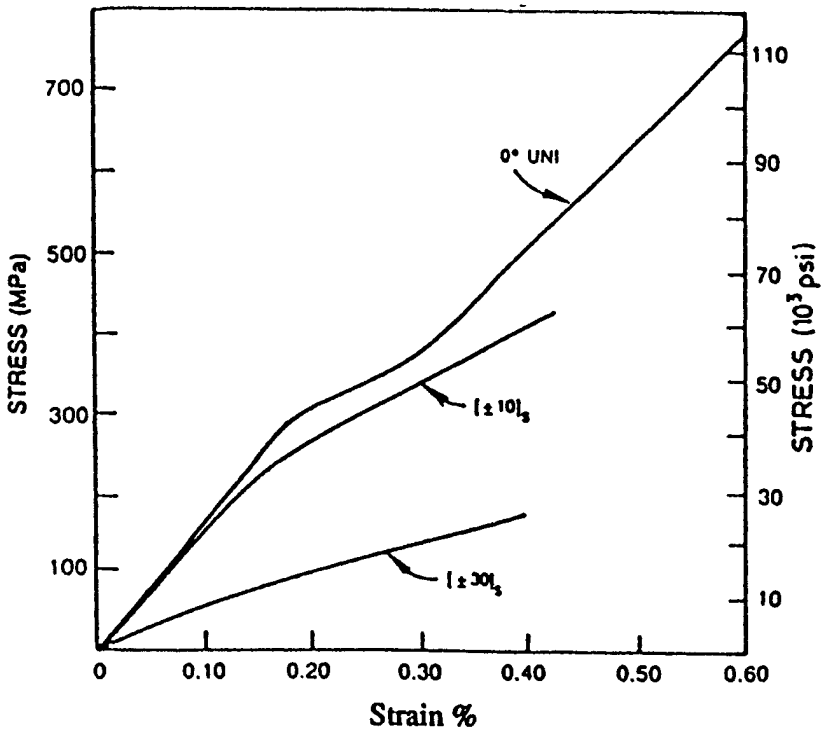

Figure 3. The Stress-Strain Response of A HMU 7740 Composite Laminate (After Ref. [2]).

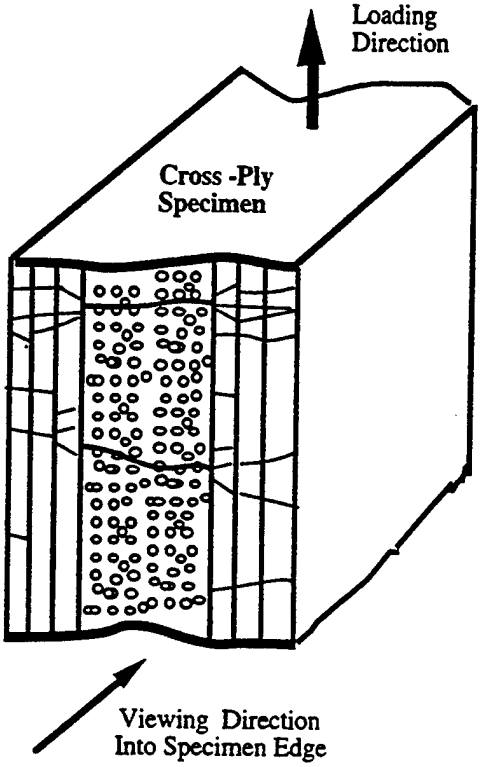

Figure 4. Damage by Transverse Matrix Cracking , with fiber-bridged cracks in the outer 0° plies, in Cross-Ply Coupons

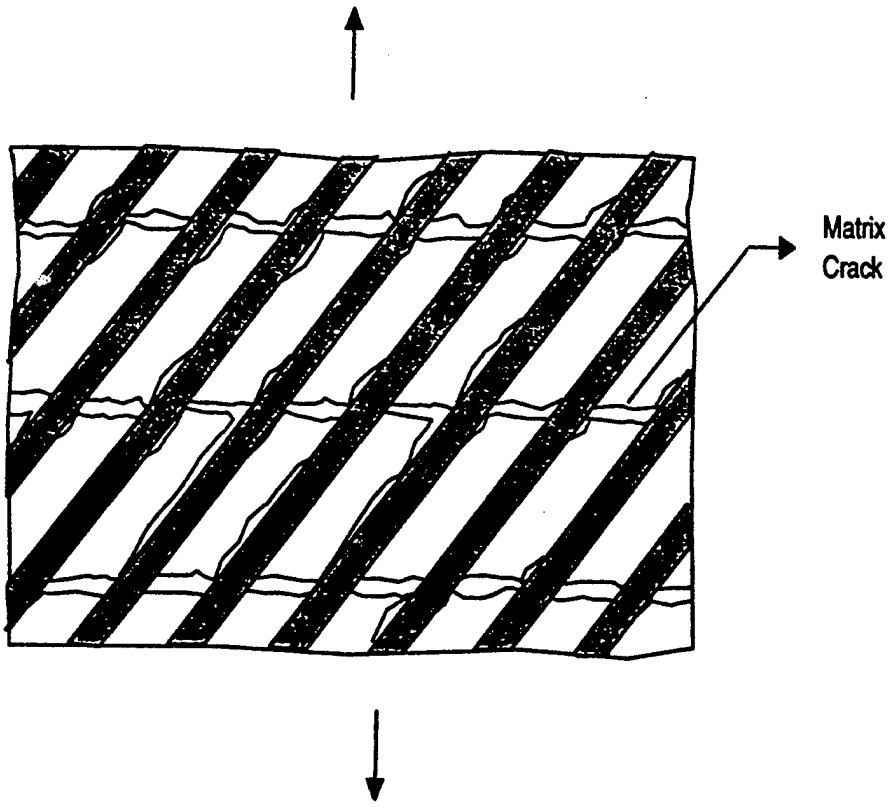

Figure 5. Observed Pattern of Cracking and Interfacial Debonds in an Off-Axis, Uniaxially Reinforced Ceramic Composite (After Ref. [3])

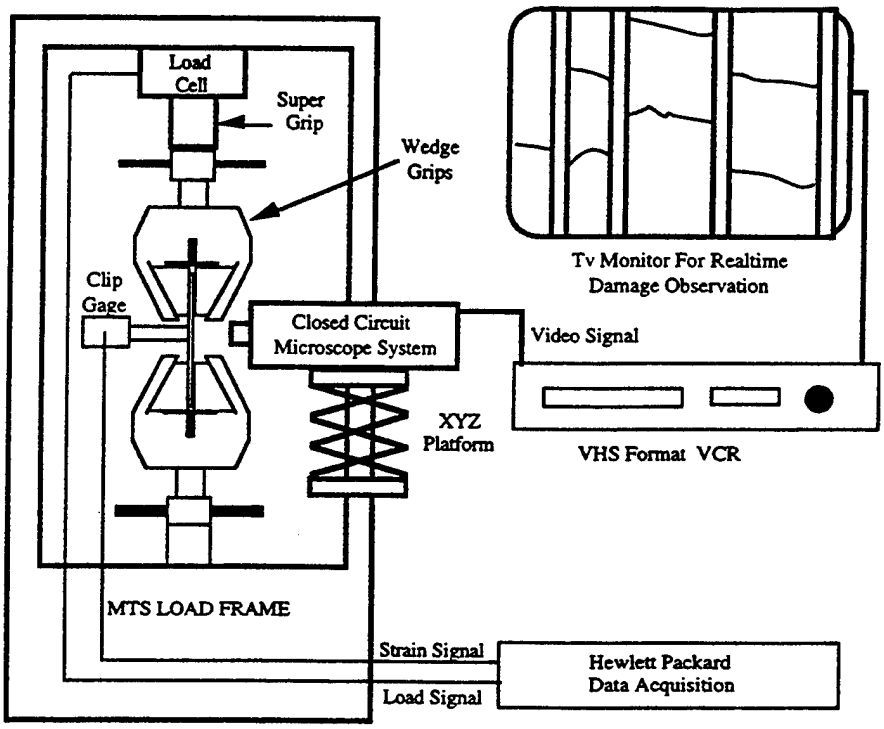

Figure 6. Experimental Set-Up

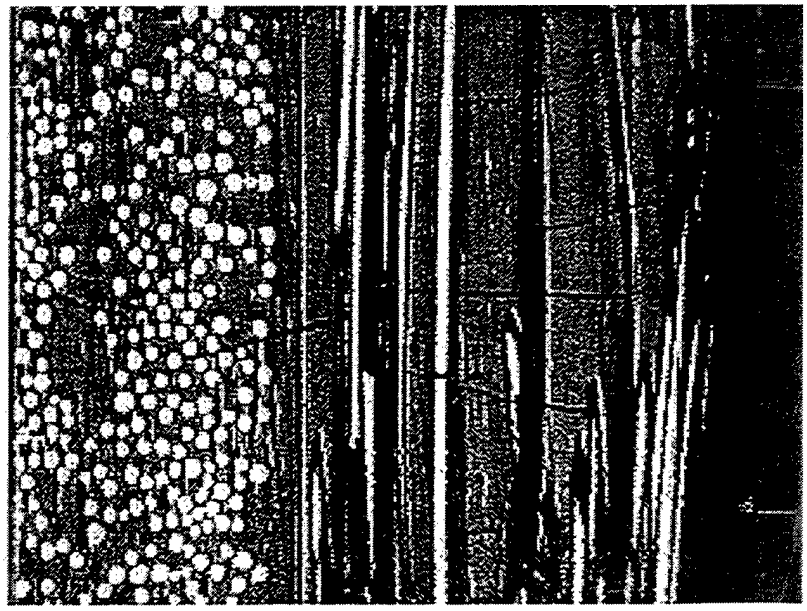

Figure 7. Typical Transverse Cracking in a Cross-Ply Laminate

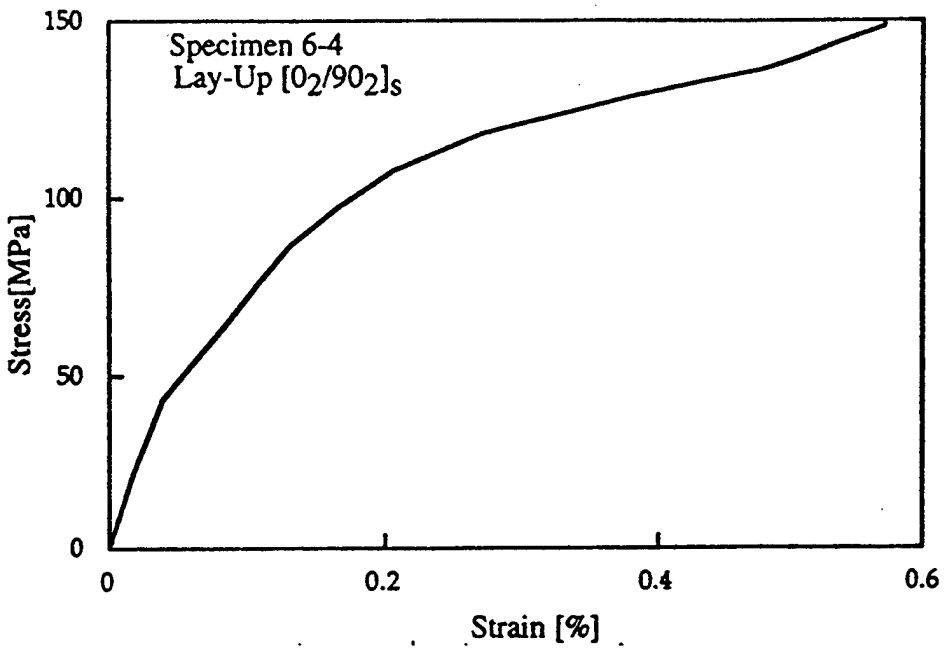

Figure 8. Stress-Strain Data for a $[0_2/90_2]_s$ Lay-Up

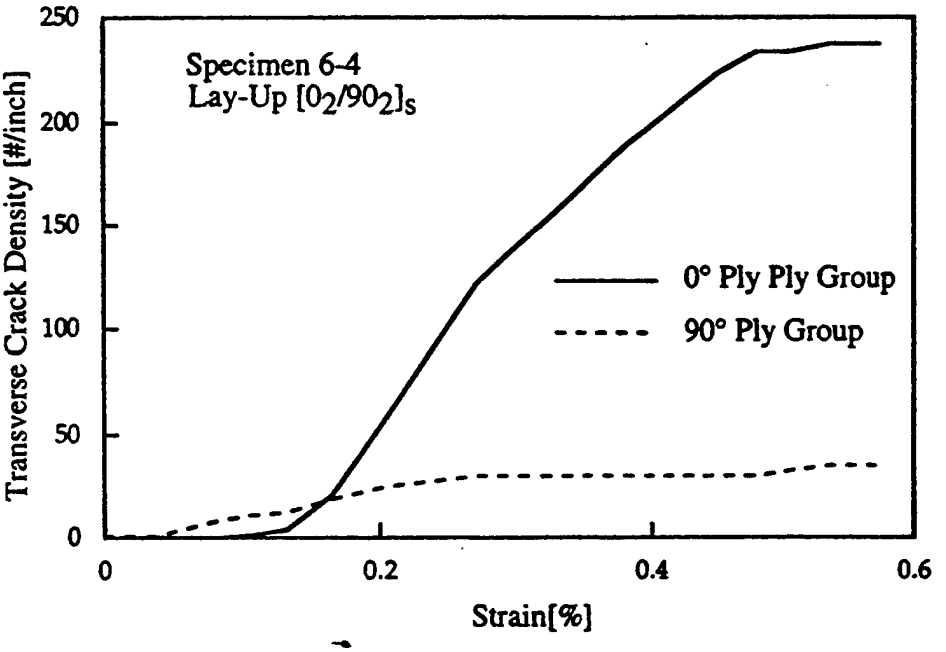

Figure 9. Countings of Crack Densities in the 0°and 90° Ply-Groups of the Coupon Related in Fig. 8

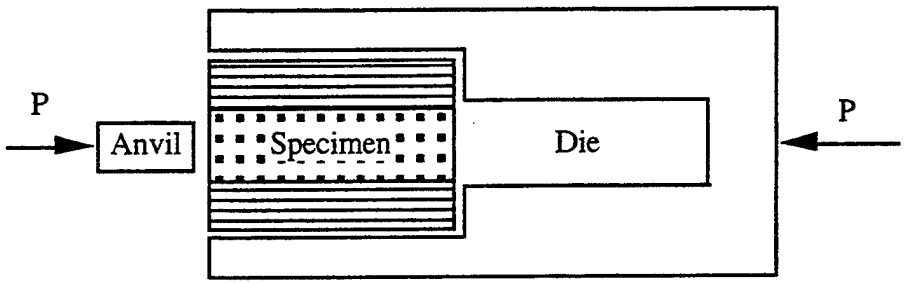

Figure 10. "Mini-Shear" Inter-Ply Strength Fixture

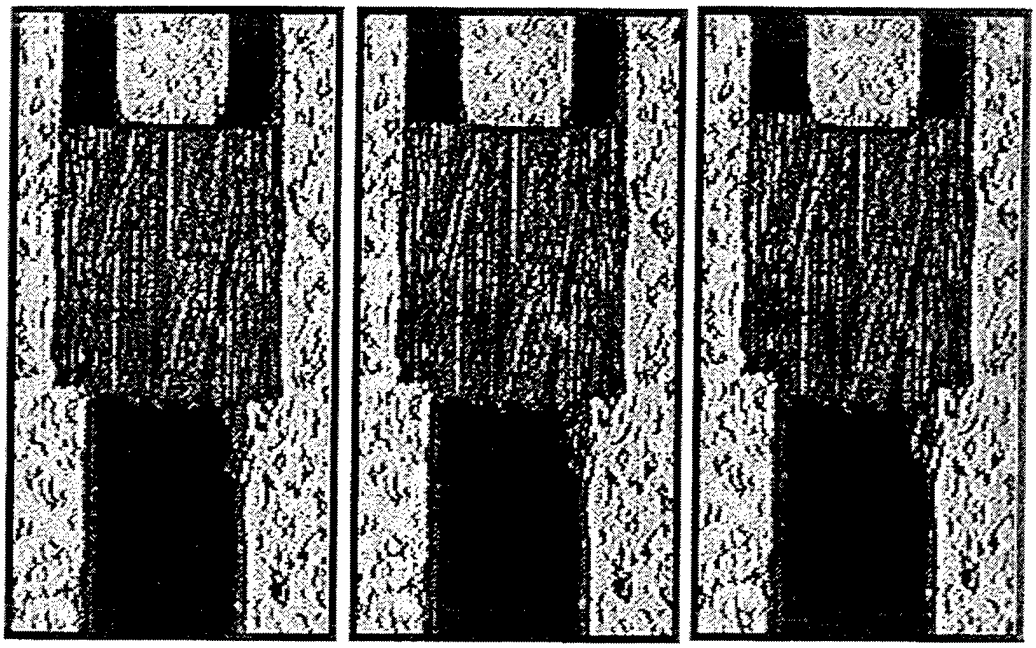

(a) (b) (c)

Figure 11. Damage Progression for the Mini-Shear Test

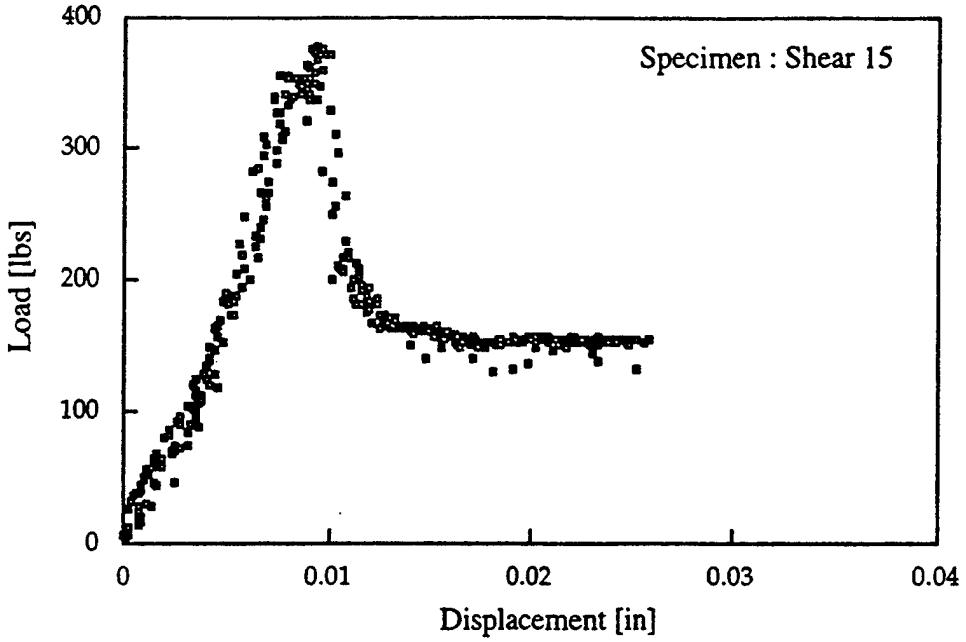

Figure 12. Load Displacement Response of the Mini-Shear Specimen

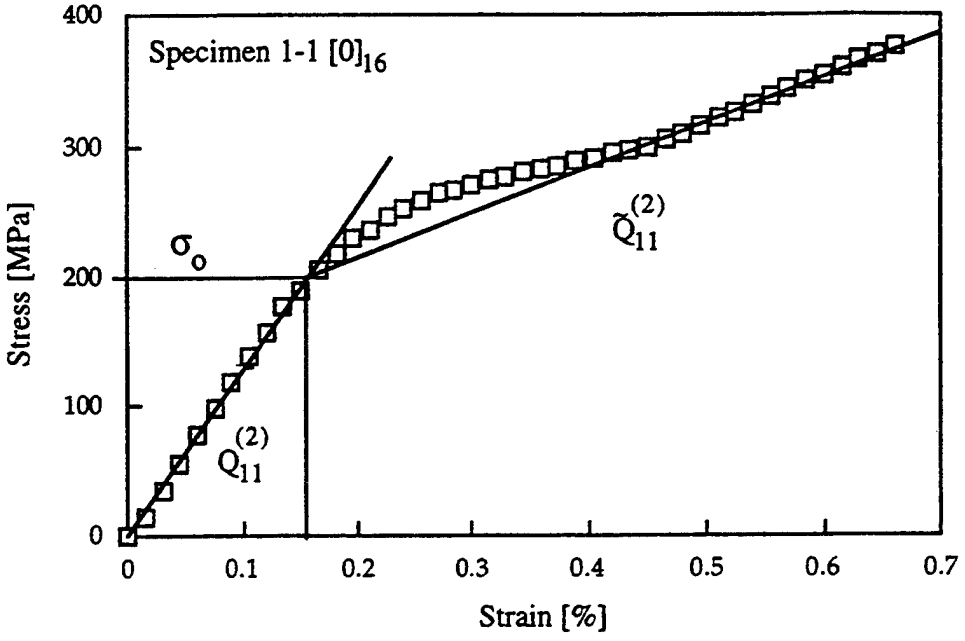

Figure 13. Bilinear Representation of the Stress-Strain Curve for a Uni-Axially (0°) Reinforced Ceramic Composite

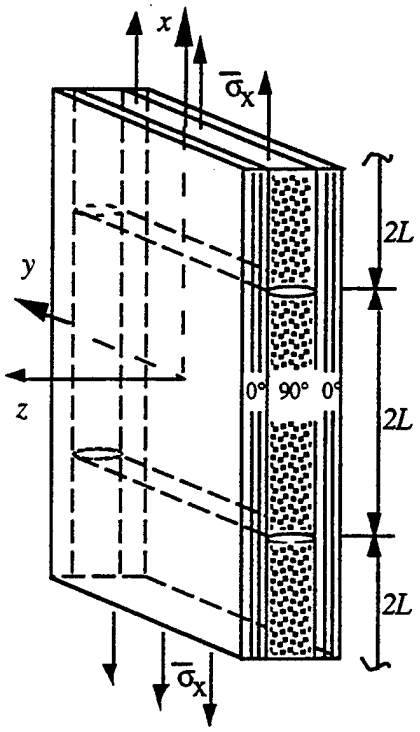

Figure 14(a): Cross-Ply Specimen Geometry

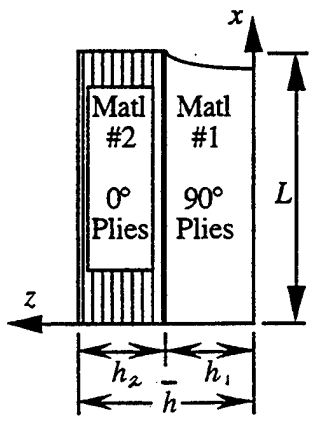

Figure 14(b): Quarter Volume Representative Element

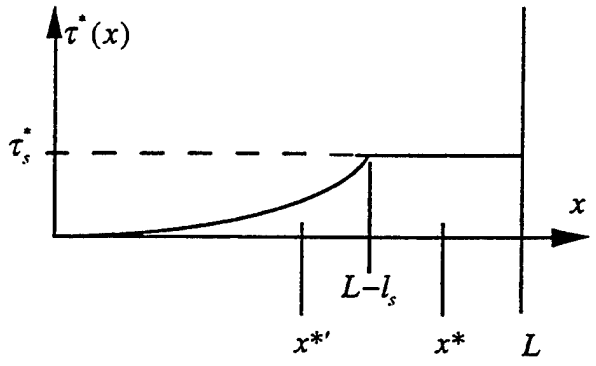

Figure 15. The three Sub-Regions of the Shear-Lag Model. Slip Occurs at $L-l_s<x<L$, While Bilinear Stress-Strain Response occurs over $x^* < x < L$. Note that x^* May Fall Within or Outside the Slip Region.

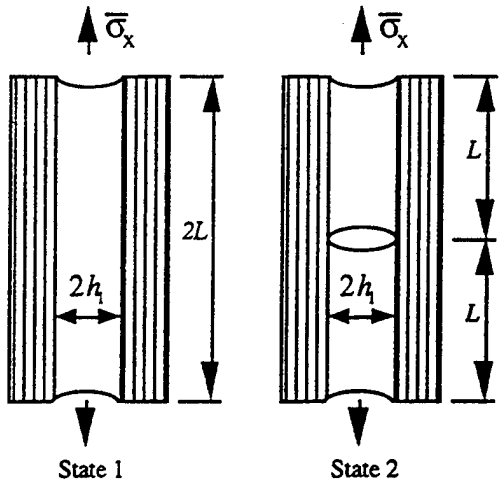

Figure 16(a): Progression of Transverse Matrix Cracks (Edge View)

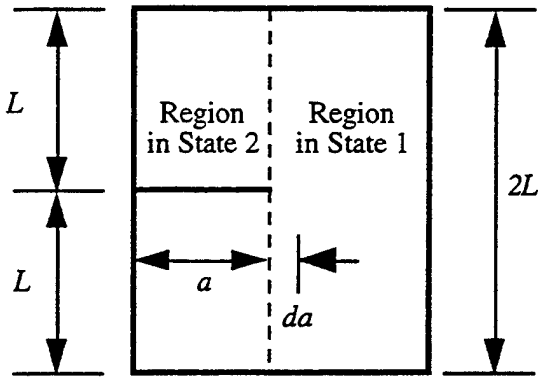

Figure 16(b): Progression of Transverse Matrix Cracks (Side View)

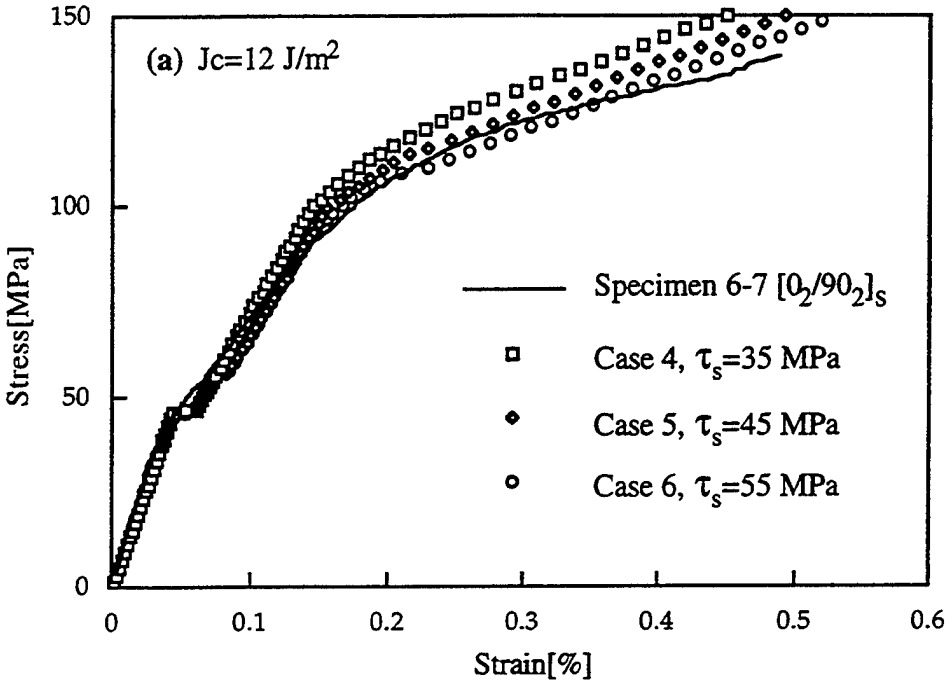

(a) Stress-Strain Response

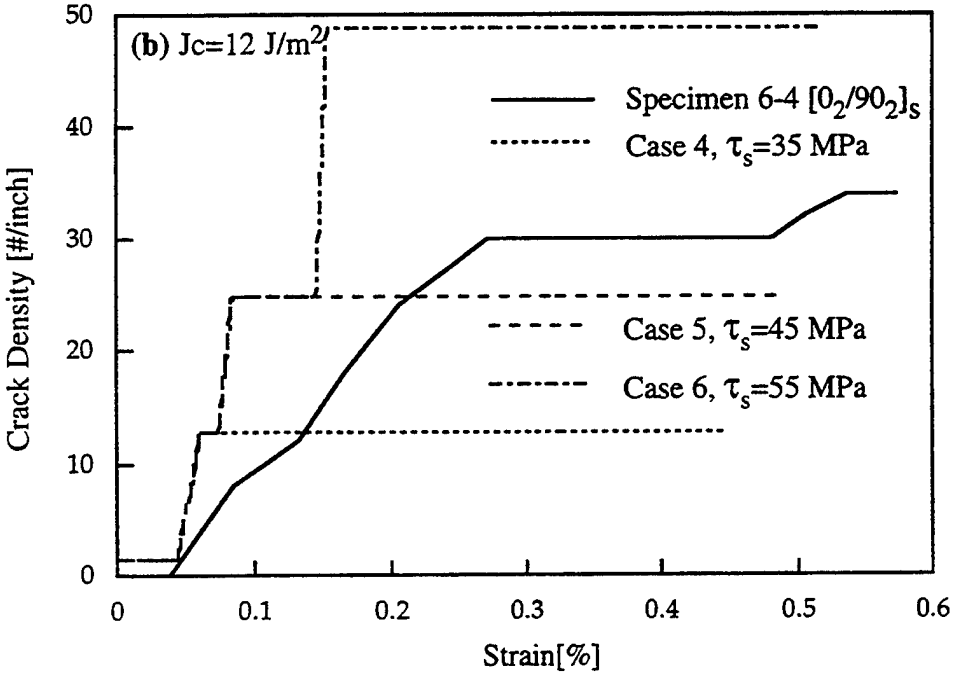

(b) Transverse Crack Density

Figure 17. Response of a $[0_2/90_2]_s$ Laminate for Bilinear Slip Analyses Case Studies, J_{IC} = 12 J/m^2

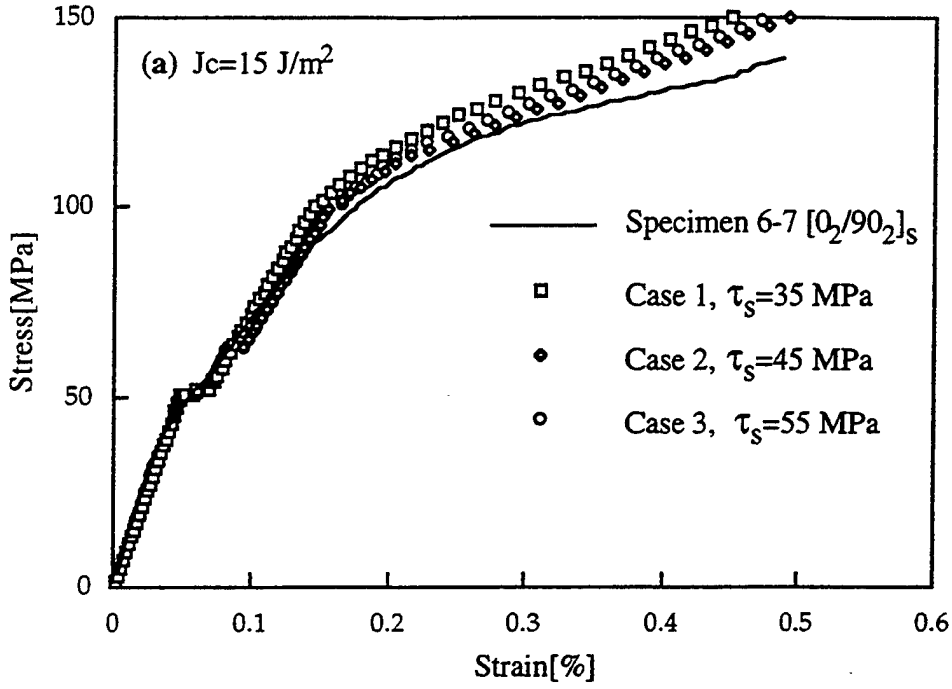

(a) Stress-Strain Response

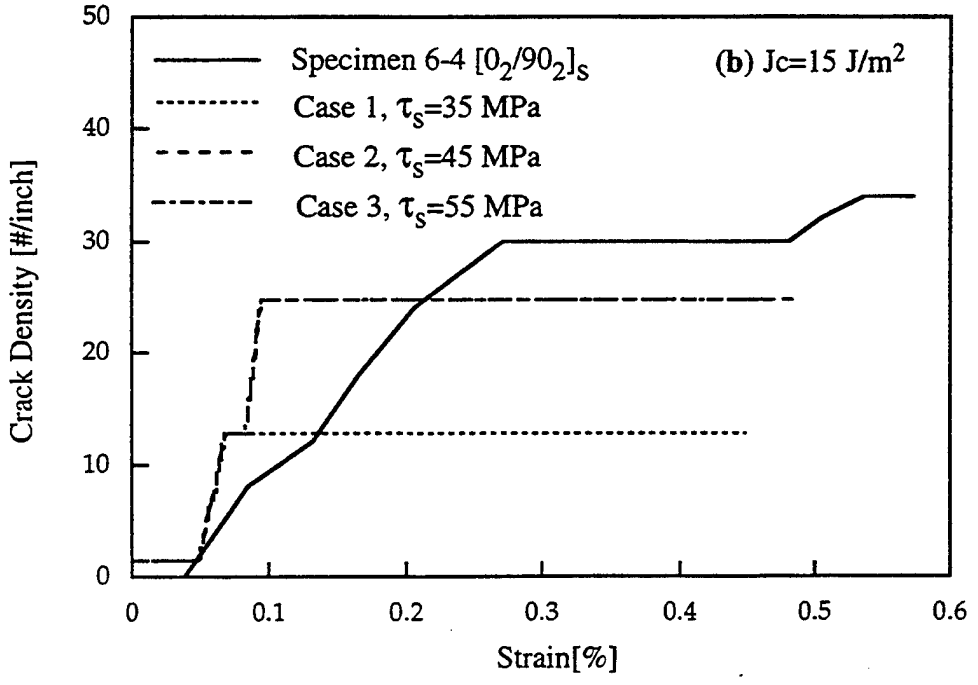

(b) Transverse Crack Density

Figure 18. Response of a $[0_2/90_2]_s$ Laminate for Bilinear Slip Analyses Case Studies, J_{IC} = 15 J/m^2

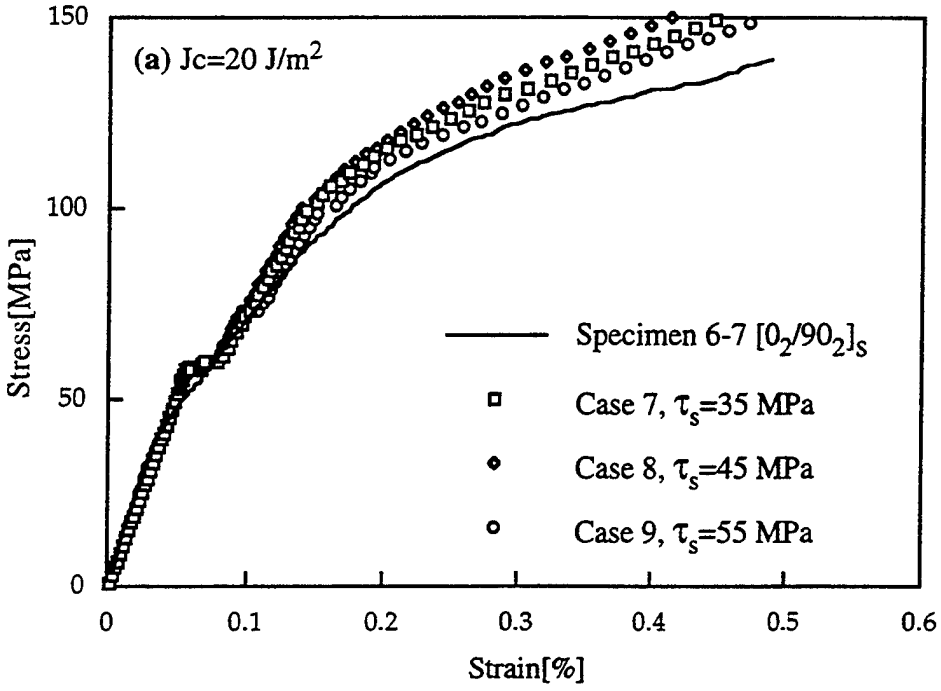

(a) Stress-Strain Response

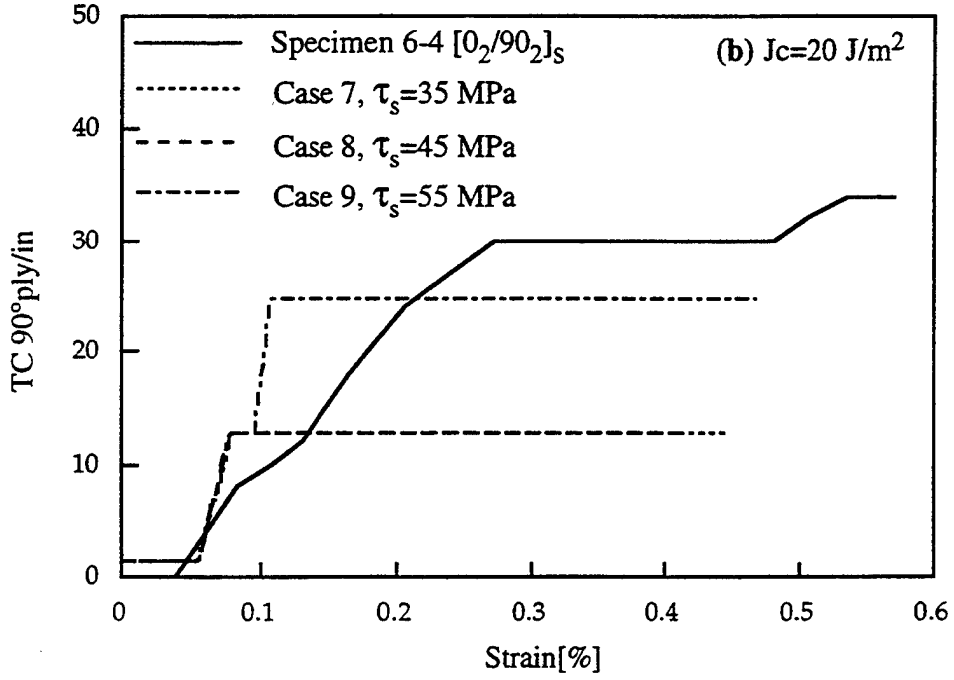

(b) Transverse Crack Density

Figure 19. Response of a $[0_2/90_2]_s$ Laminate for Bilinear Slip Analyses Case Studies, J_{IC} = 20 J/m^2

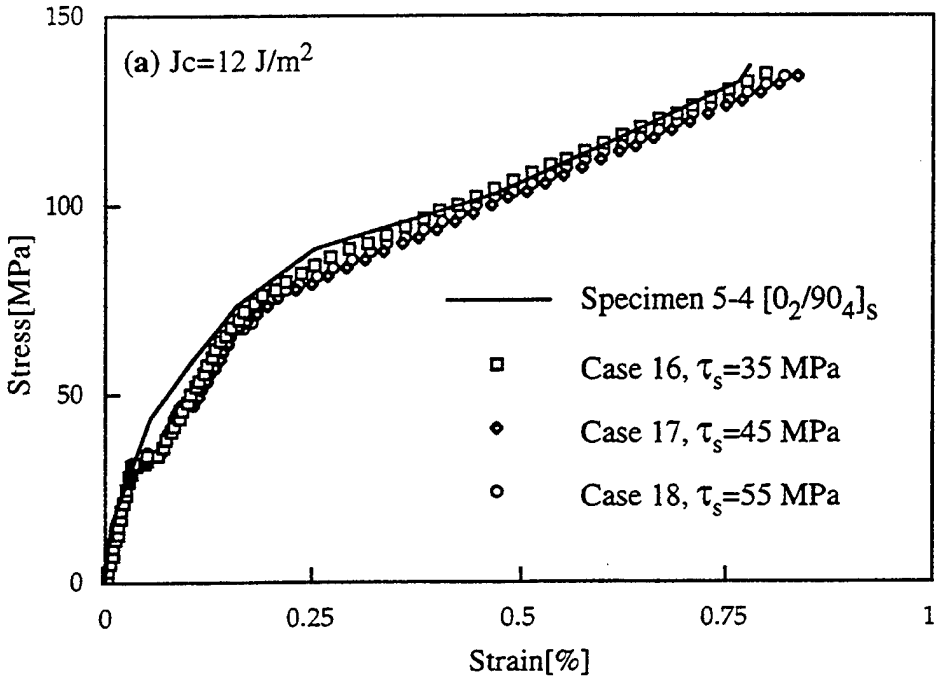

(a) Stress-Strain Response

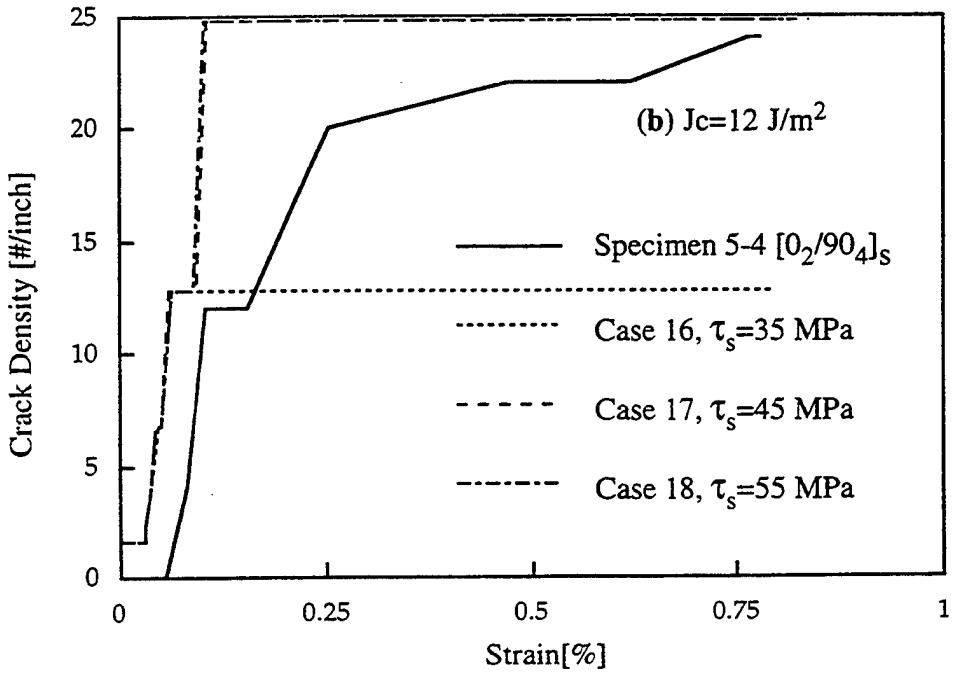

(b)Transverse Crack Density

Figure 20. Response of a $[0_2/90_4]_s$ Laminate for Bilinear Slip Analyses Case Studies, J_{IC} = 12 J/m^2

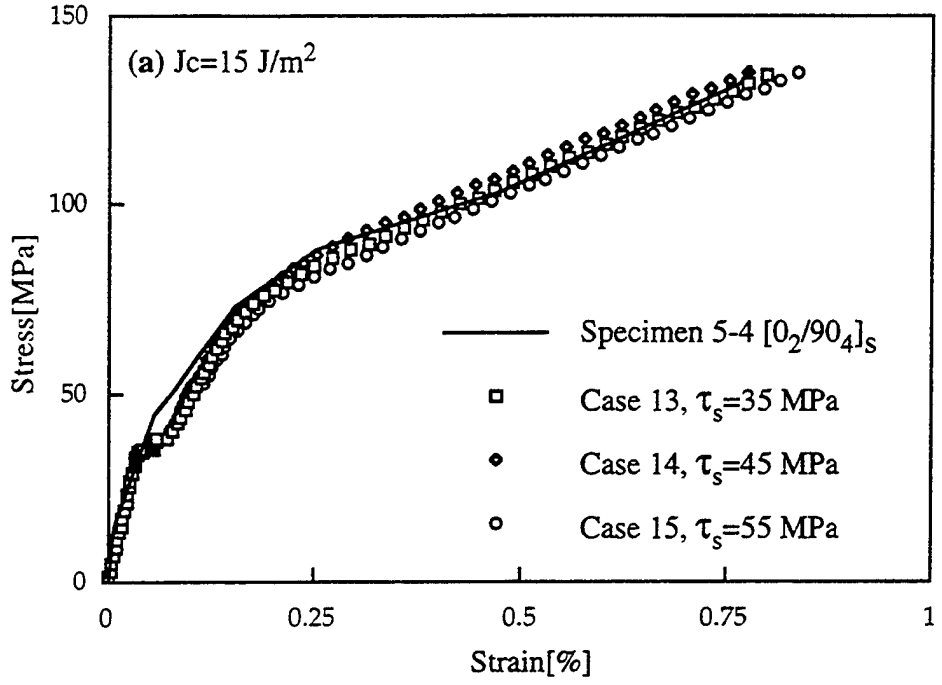

(a) Stress-Strain Response

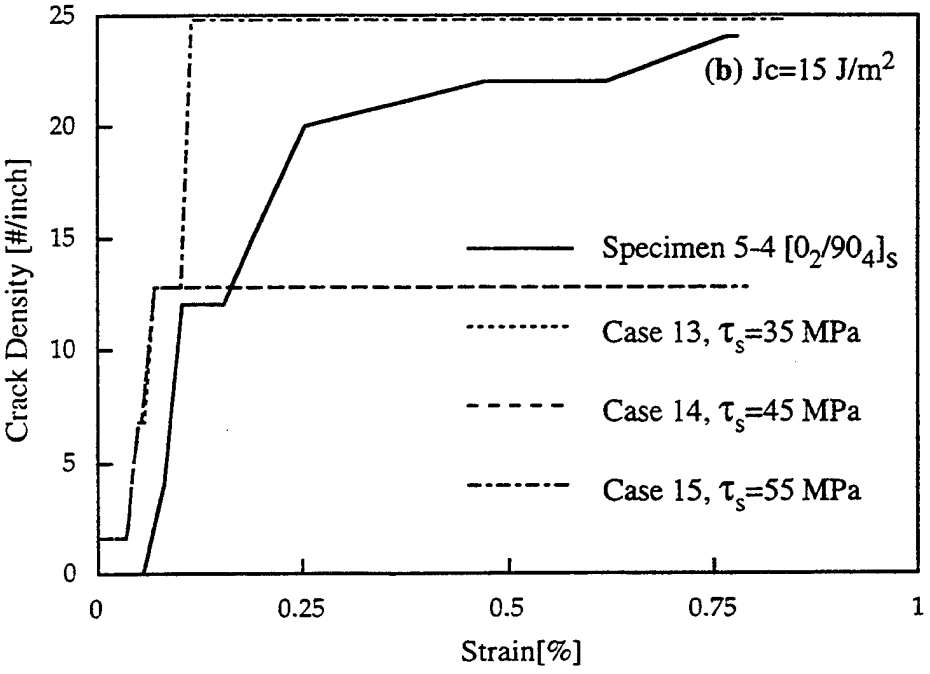

(b) Transverse Crack Density

Figure 21. Response of a $[0_2/90_4]_s$ Laminate for Bilinear Slip Analyses Case Studies, J_{IC} = 15 J/m^2

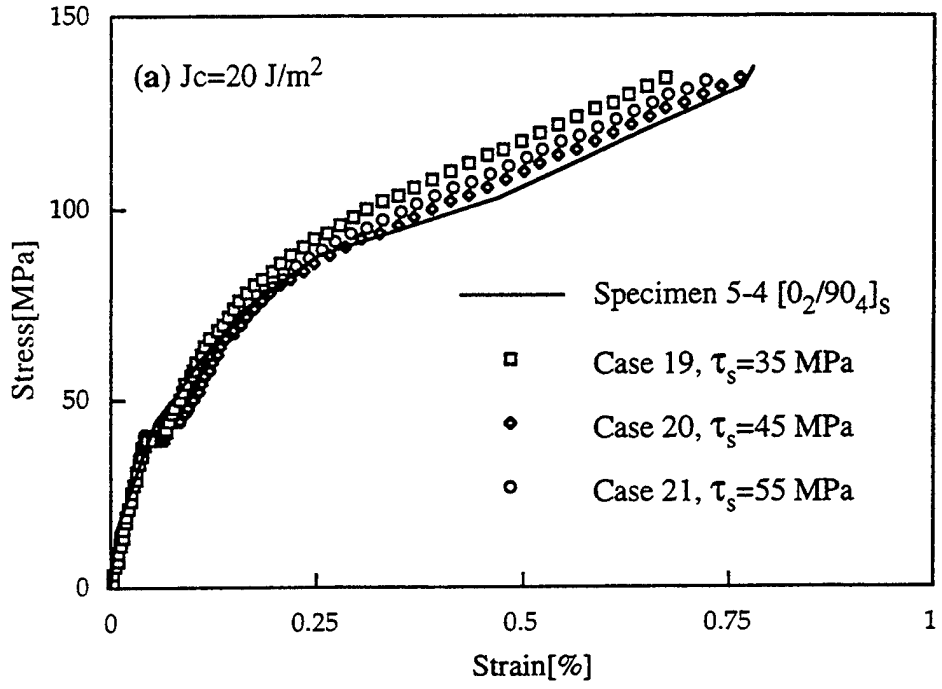

(a) Stress-Strain Response

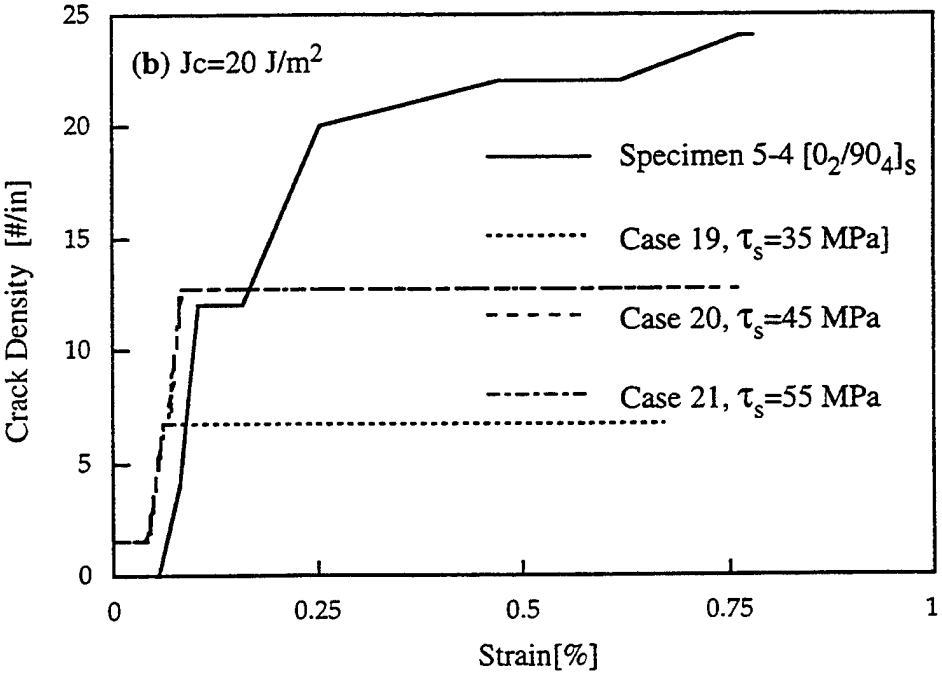

(b) Transverse Crack Density

Figure 22. Response of a $[0_2/90_4]_s$ Laminate for Bilinear Slip Analyses Case Studies, J_{IC} = 20 J/m^2

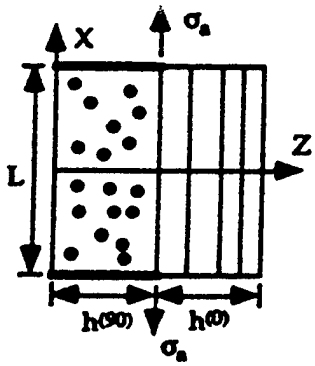

Figure 23(a): State A

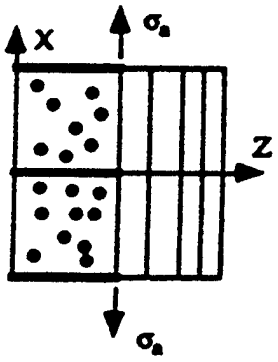

Figure 23(b): State B

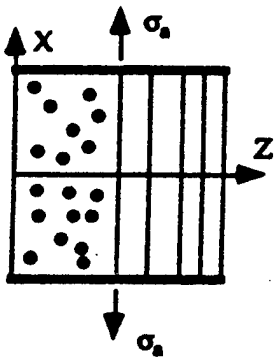

Figure 23(c): State C

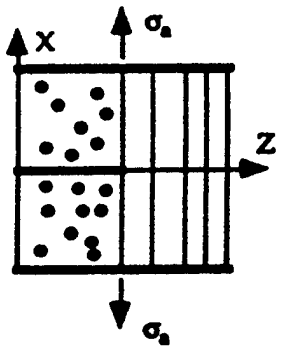

Figure 24(a): State D

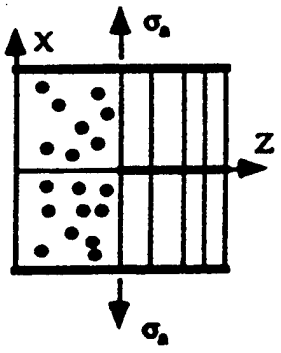

Figure 24(b): State E

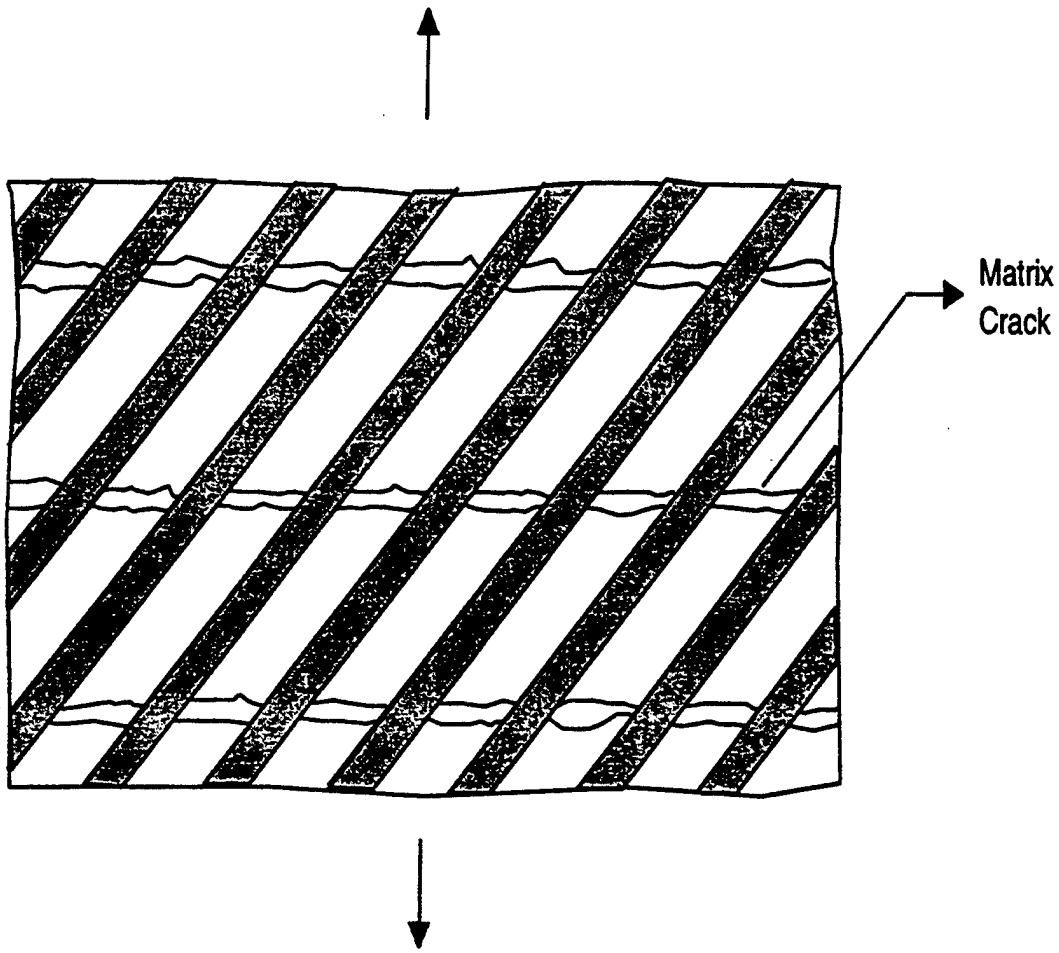

Figure 25(a): Fiber Bridged Matrix Crack at Saturation Stress σ_s

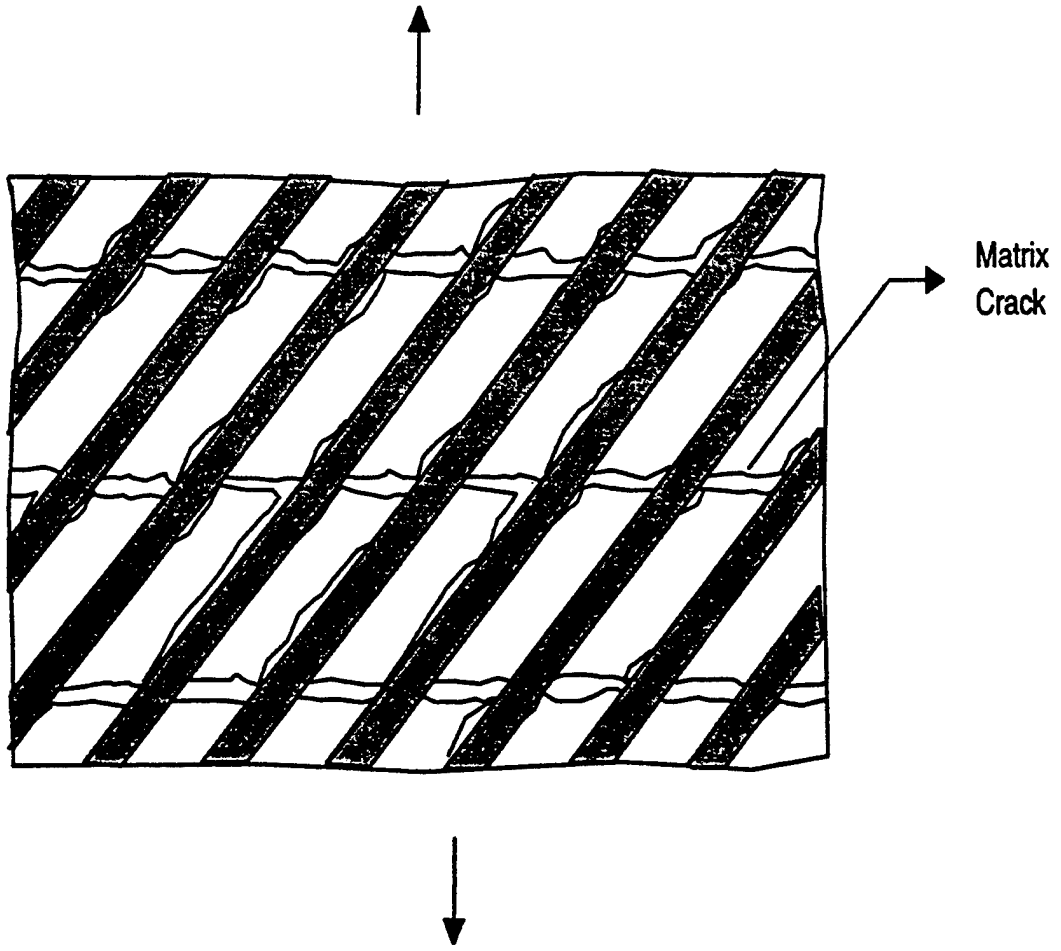

Figure 25(b): Observed Pattern of Cracking and Interfacial Debonds in an Off-Axis, Uniaxially Reinforced Ceramic Composite Under $\sigma > \sigma_s$

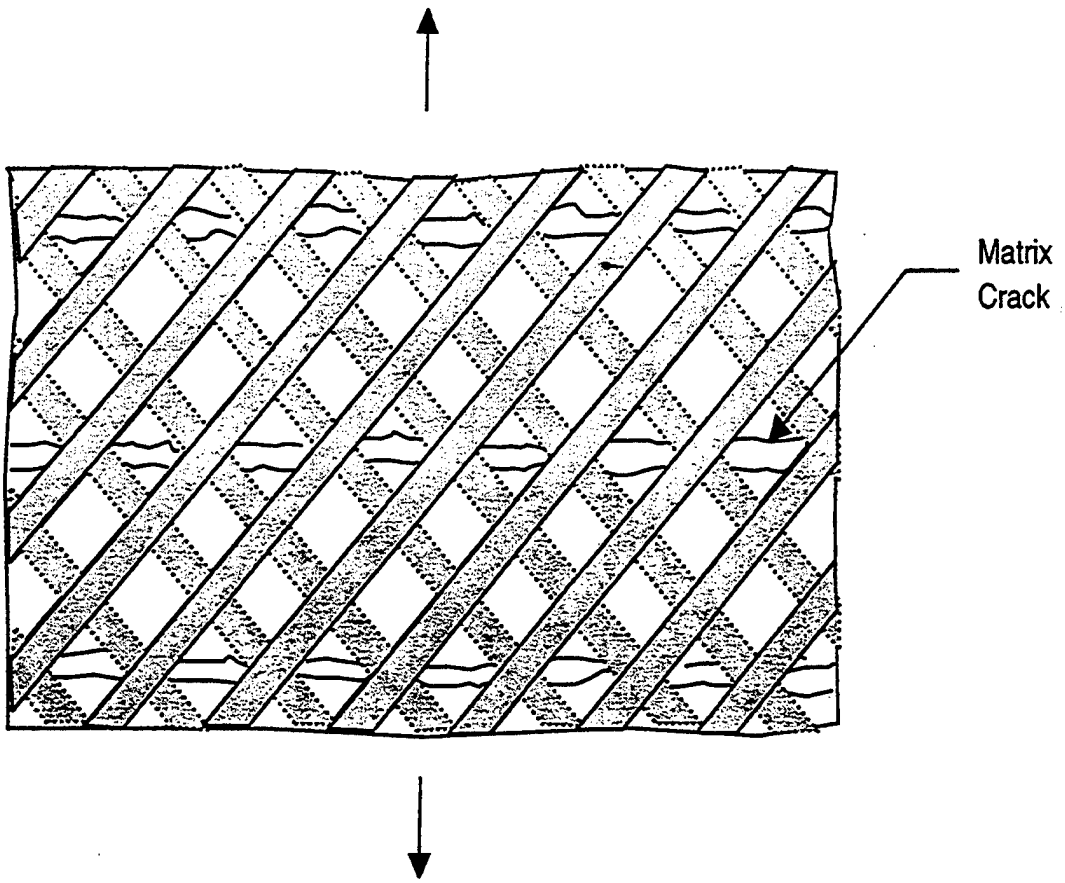

Figure 26. A Schematic Drawing of Fiber Bridged Matrix Cracks in Angle-Ply Reinforced Ceramic Composite (Sketched after Ref. [10])

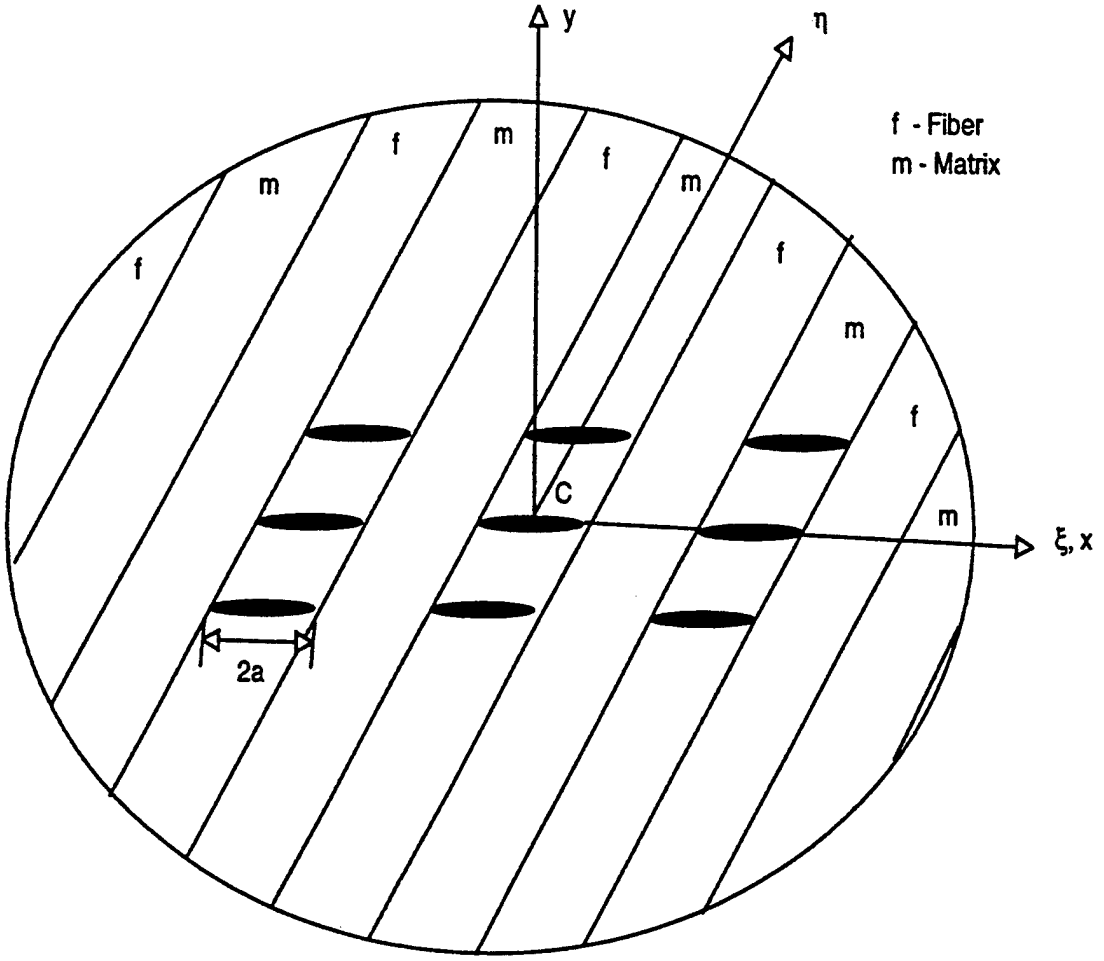

Figure 27. A System of Nine Cracks with the Representative Central Crack C

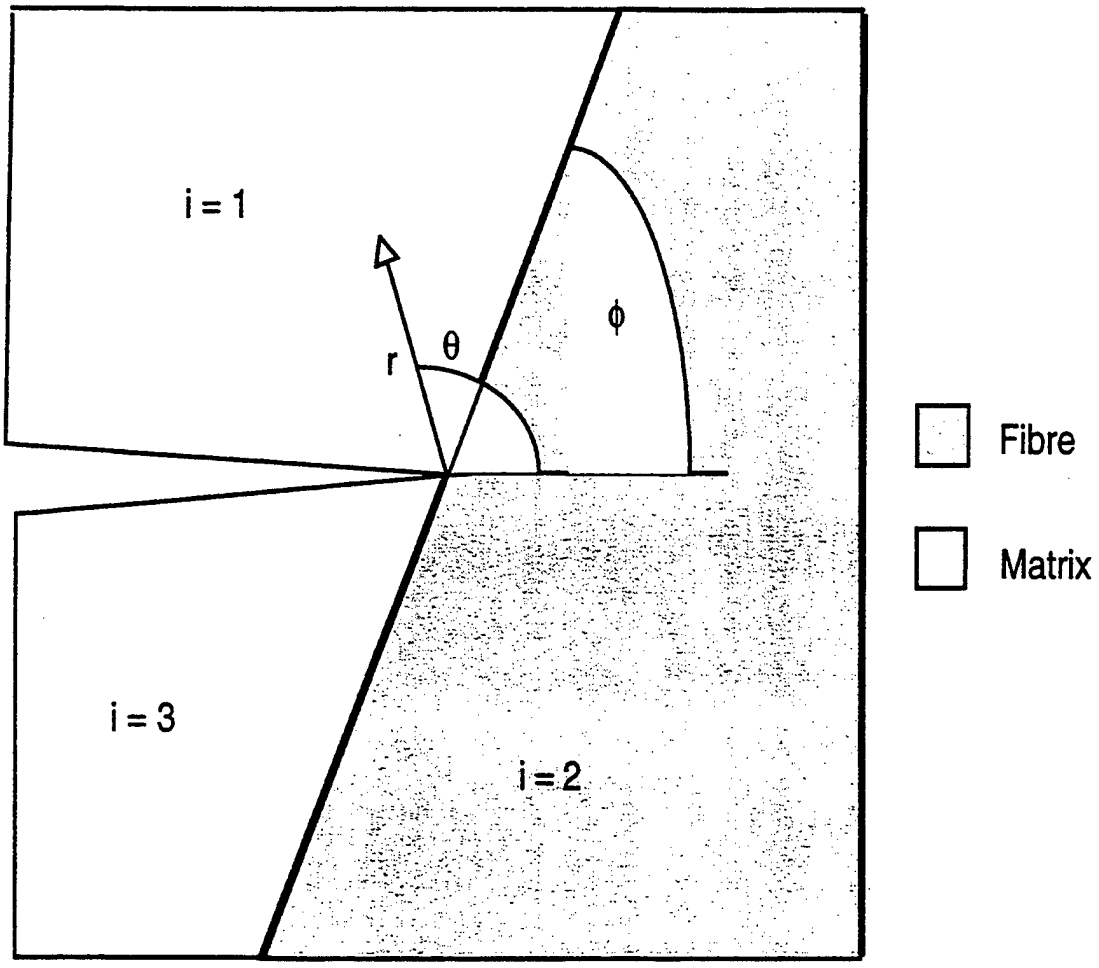

Figure 28. Geometry of the Problem as Discussed in the Eigen Function Analysis

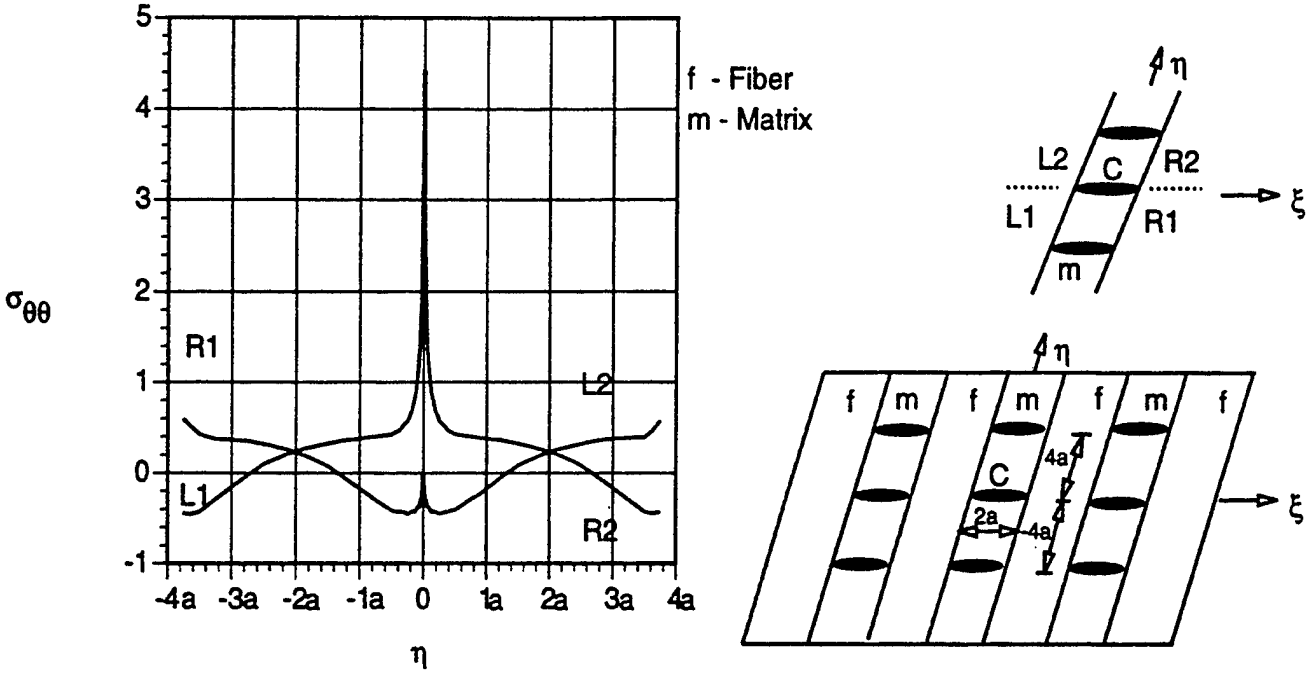

Figure 29. Variation of the Normalized Interfacial Normal Stress ($\sigma_{\theta\theta}$) Emanating from the Tip of the Central Crack, as a Function of η (ξ = a) for the Nine Crack Geometry

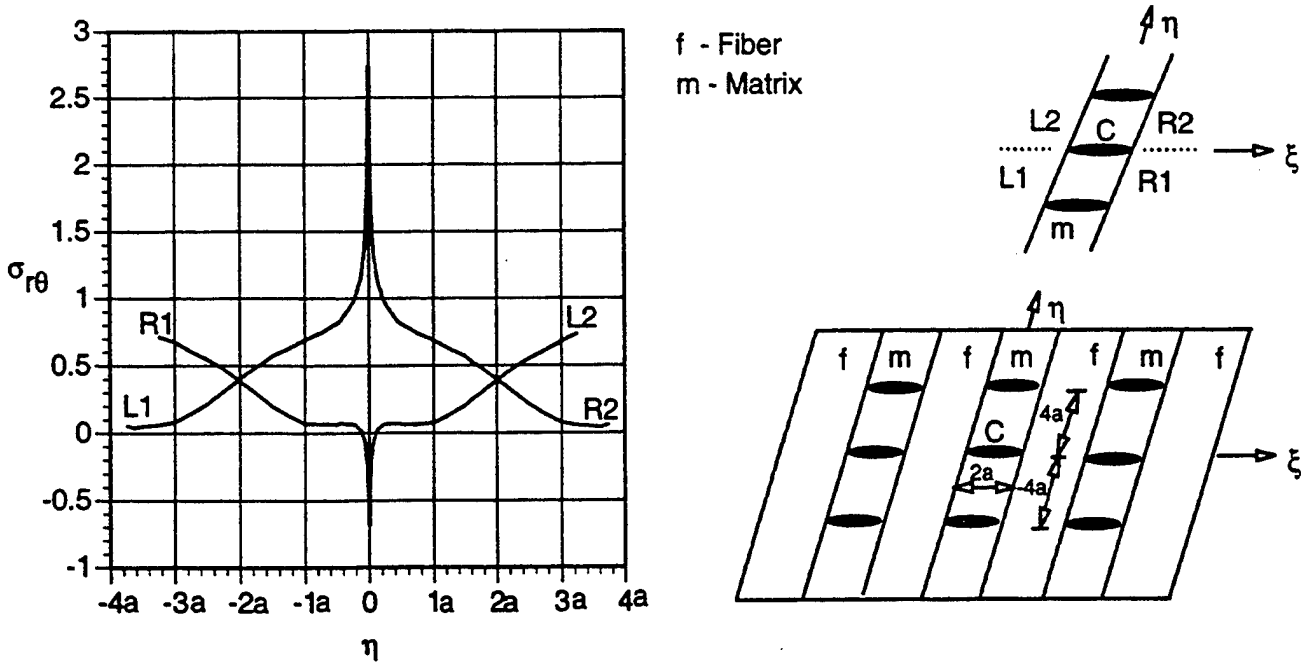

Figure 30. Variation of the Normalized Interfacial Shear Stress ($\sigma_{r\theta}$) Emanating from the Tip of the Central Crack, as a Function of η (ξ = a) for the Nine Crack Geometry

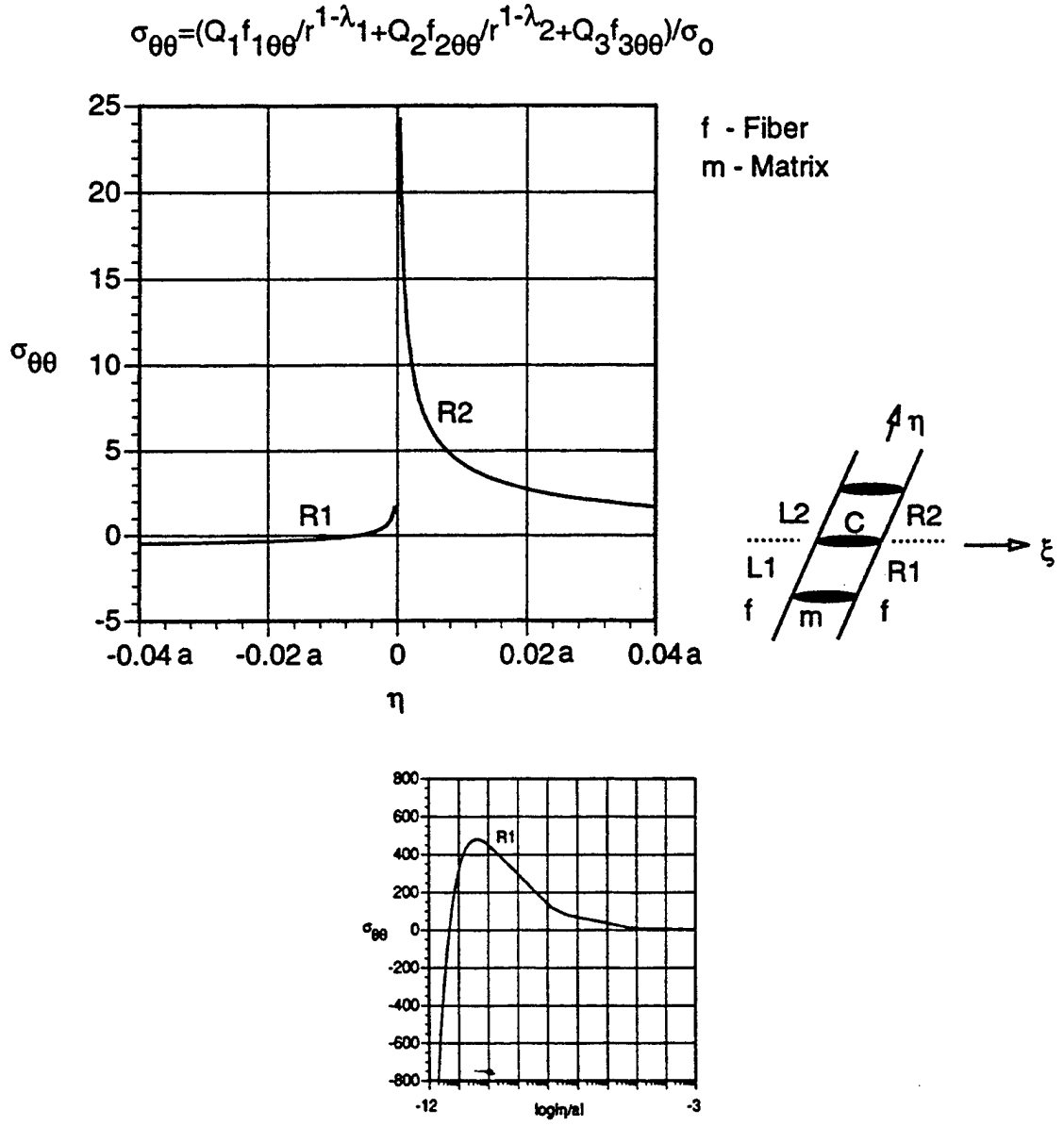

Figure 31. Variation of the Normalized Asymptotic Near Crack-Tip Interfacial Normal Stress ($\sigma_{\theta\theta}$) Emanating from the Tip of the Central Crack, as a Function of η ($\xi = a$) for the Nine Crack Geometry Sketched in Figures 27 and 29

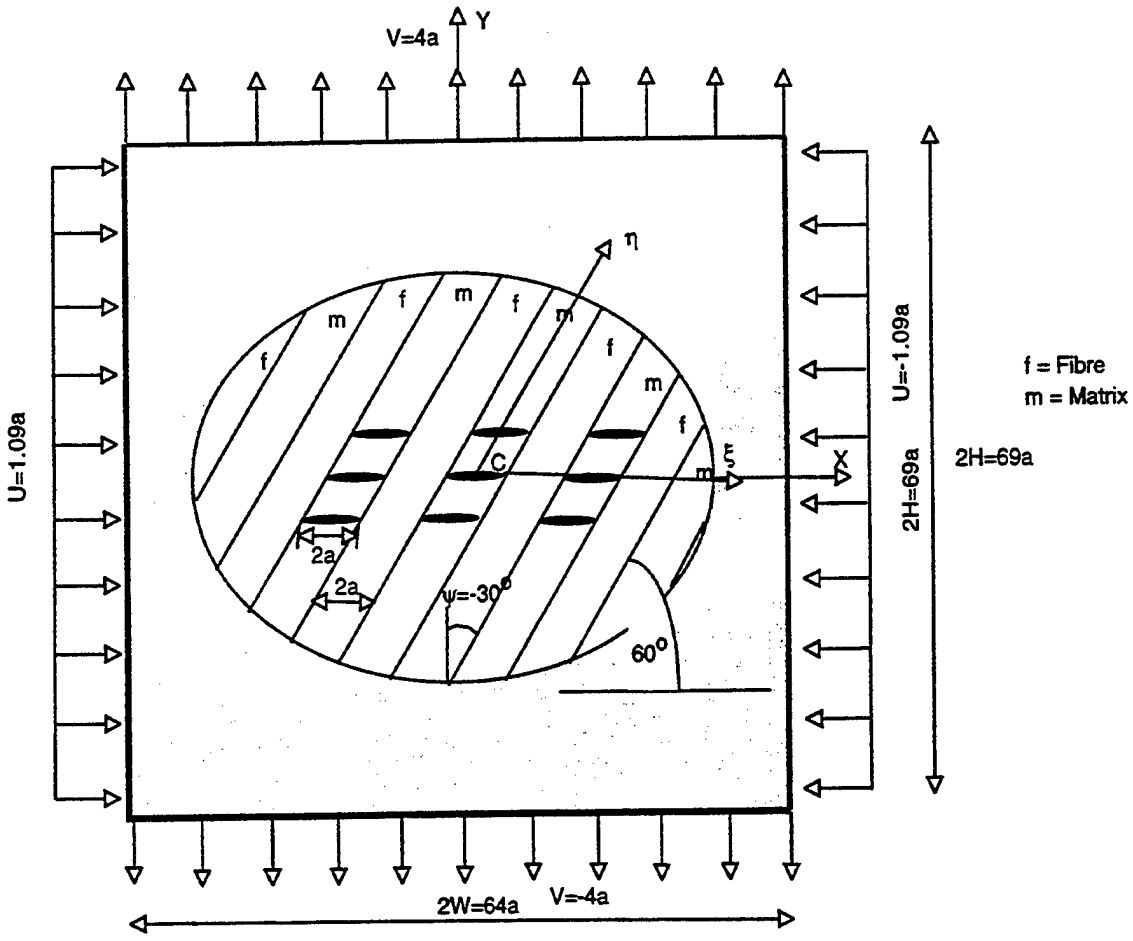

Figure 32. The Geometry of the Nine Matrix Crack in the $\psi = -30^{\circ}$ ply

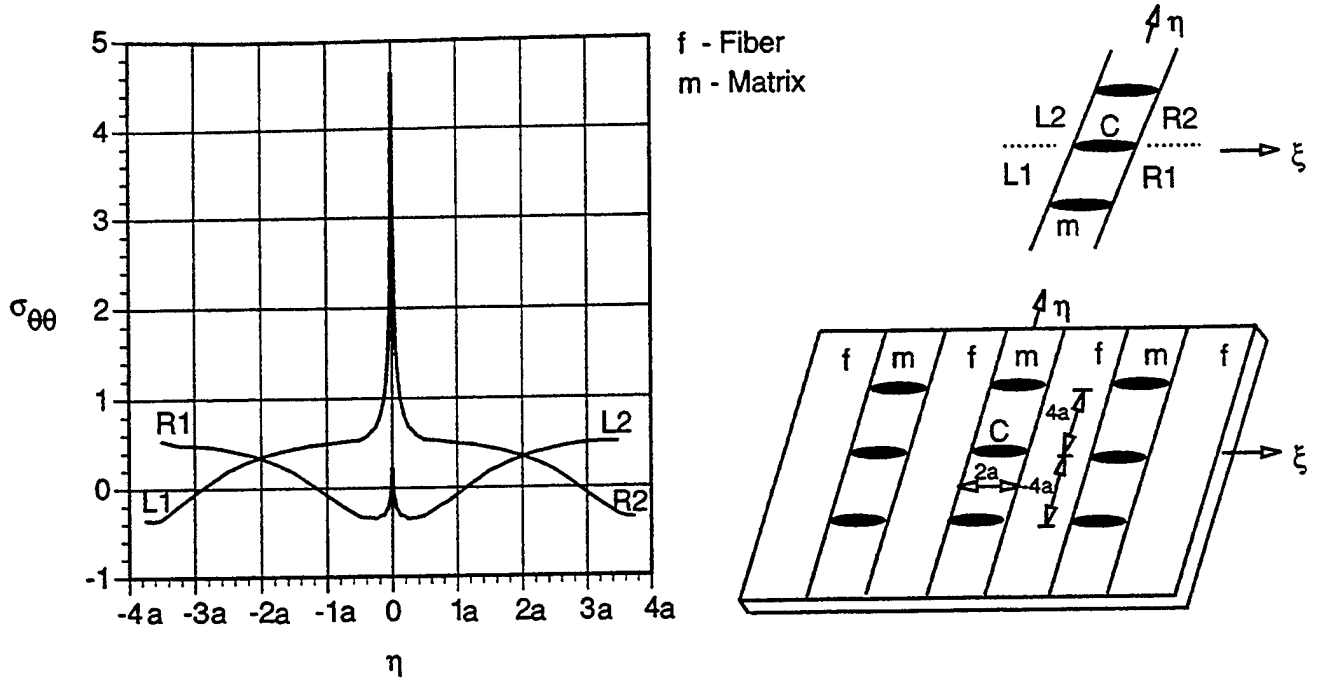

Figure 33. Variation of the Normalized Interfacial Normal Stress ($\sigma_{\theta\theta}$) Emanating from the Tip of the Central Crack, as a Function of η (ξ = ±a) for the Nine Crack Geometry in the ψ = -30° ply

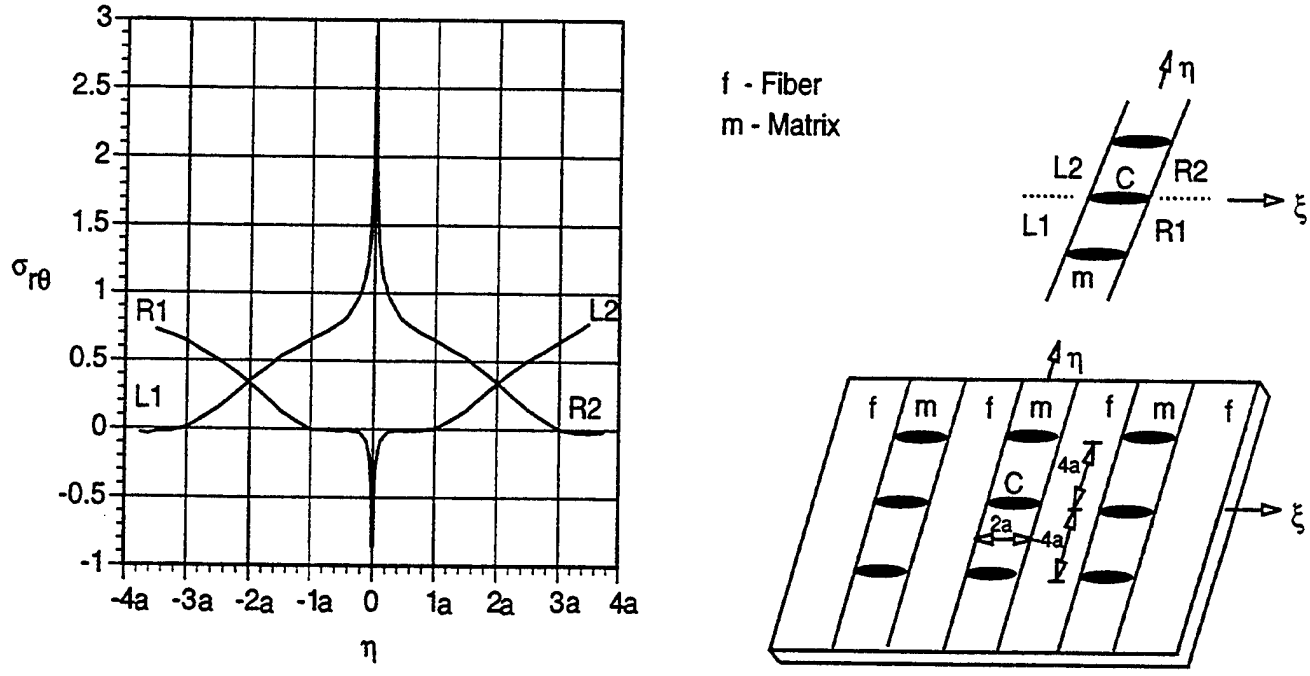

Figure 34. Variation of the Normalized Shear Stress ($\sigma_{r\theta}$) Emanating from the Tip of the Central Crack, as a Function of η (ξ = ±a) for the Nine Crack Geometry in the ψ = -30° ply

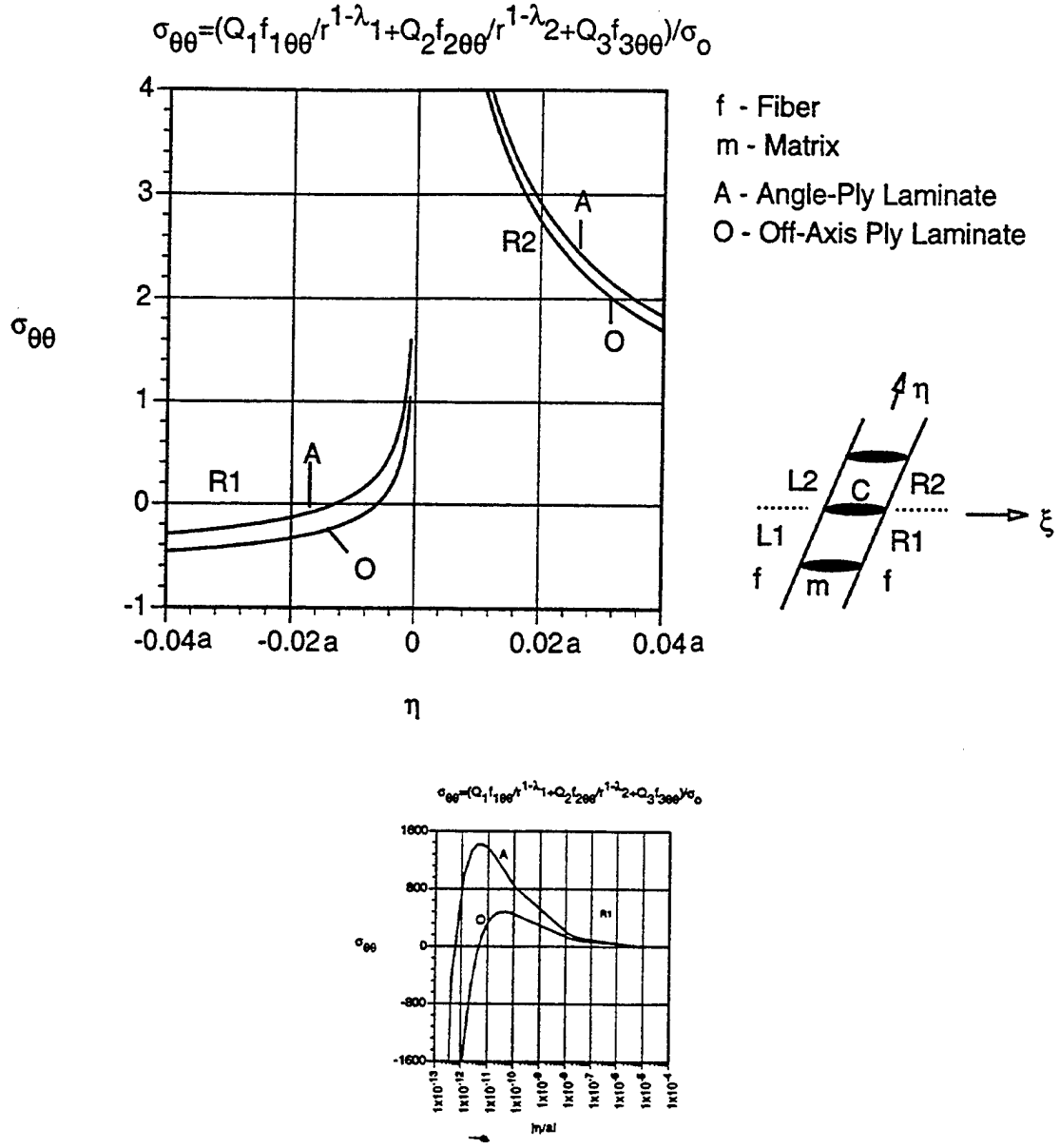

Figure 35. Variation of the Normalized Asymptotic Near Crack-Tip Interfacial Normal Stress ($\sigma_{\theta\theta}$) Emanating from the Tip of the Central Crack, as a Function of η ($\xi = \pm a$) for the Nine Crack Geometry Sketched in Figure 27 in the $\psi = -30^{\circ}$ ply

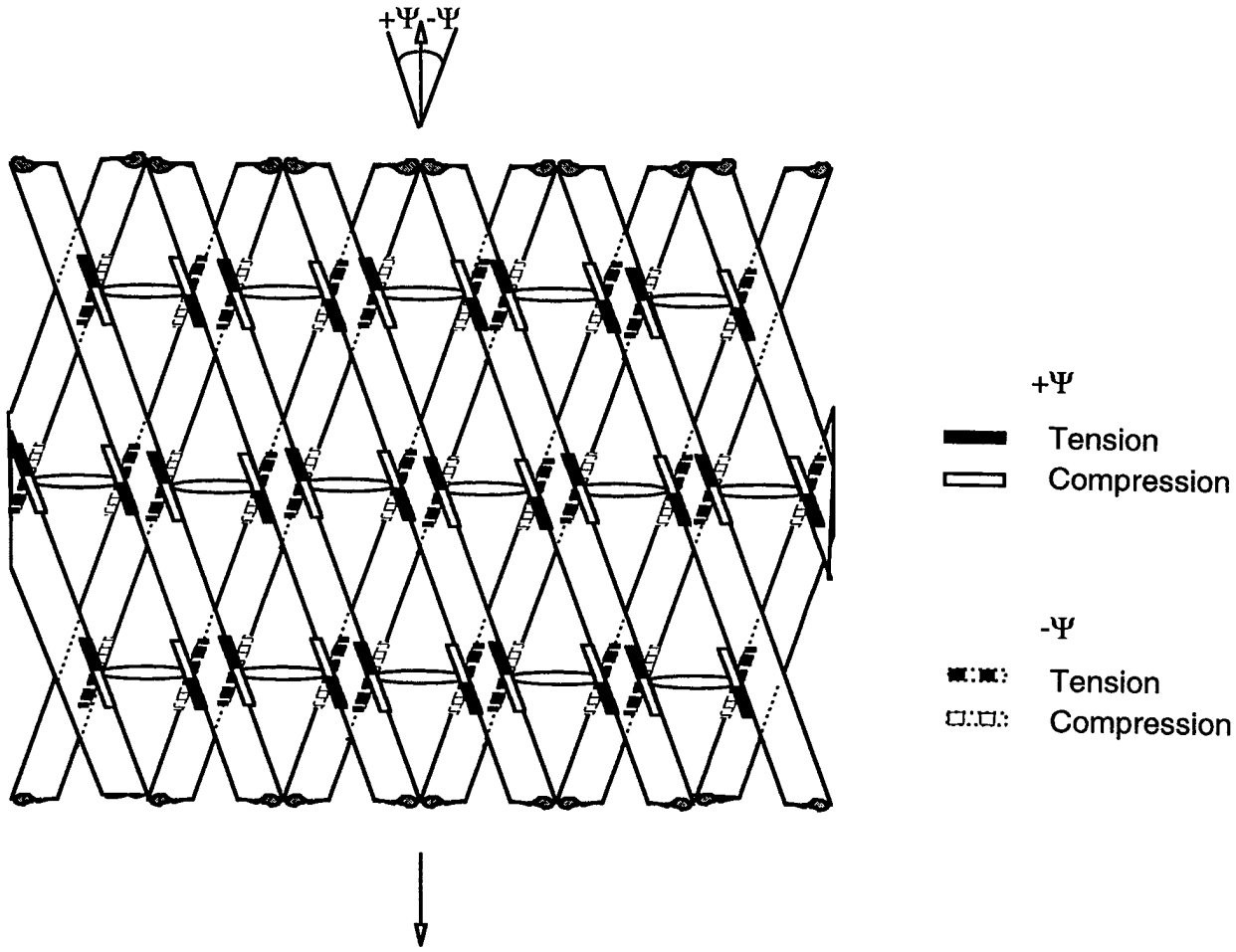

Figure 36. Regions of Interfacial Fiber/Matrix Tensile and Compressive Tractions in $a[\pm\psi]_s$ Angle-Ply Laminate. Note that Debondings in the $(+\psi)$ Ply are Inhibited by the Fibers in the $(-\psi)$ Ply and Vice Versa